Master's Thesis

Investigation and Comparison Between Radiation and Phase Center for Canonical Antennas

Casimir Ehrenborg

Department of Electrical and Information Technology,
Faculty of Engineering, LTH, Lund University, June 2014.

Investigation and Comparison Between Radiation and Phase Center for Canonical Antennas

Casimir Ehrenborg
atf09ceh@student.lu.se

Ericsson AB
Lindholmspiren 11
417 56 Göteborg

Advisor: Gerhard Kristensson, Jonas Fridén

June 18, 2014

Printed in Sweden
E-huset, Lund, 2014

Abstract

The phase center is defined as the point on an antenna from which the far field radiation seems to originate. Phase center calculations are often uncertain and vague, and very little concrete information is available on the subject. Recently, a replacement parameter called the radiation center was introduced in [5]. The radiation center is more rigorously defined than the phase center and possesses additional qualities, such as uniqueness, no need for user input, etc. This thesis evaluates the validity of the radiation center as a replacement for the phase center and also compares it with Muehldorf's analytically calculated phase center [17]. The far-field is simulated in CST and evaluated in Matlab, using Ericsson Antenna Model Library (eamlib) to calculate the radiation center. Phase center calculations are carried out in CST and the Muehldorf phase center is evaluated numerically in Matlab.

The radiation center minimizes the phase well, achieving the same smoothness as the phase center. The radiation center varies according to the predicted behaviour of the phase center for most antennas. For the spiral antenna the radiation center does not adhere to the predicted behaviour of the phase center. For some antennas, specifically those that have wide or narrow beam widths in a certain direction, the radiation center seems to mainly be influenced by the phase function in the plane with wider radiation pattern. This strengthens the theoretical argument in [5] that the radiation center minimizes the phase according to far-field amplitude. The radiation center produces results within the bounds of the antenna structure for all antennas presented in this thesis. In contrast the phase center does not, specifically for the Yagi-Uda antenna and the Leaky Lens antenna [18]. The phase function in the main radiation lobe is regarded explicitly for some of the simulated antennas. The radiation center does not seem to minimize the phase for these antennas any better or worse than the phase center. These results suggest that the radiation center is a good candidate for origin of radiation for antennas.

Table of Contents

Acronyms

AUT	Antenna Under Test
CST	Computer Simulation Technology
eamlib	Ericsson Antenna Model Library
HPBW	Half Power Beam Width
IEEE	Institute of Electrical and Electronics Engineers
SWE	Spherical Wave Expansion

Table 0.1: Acronyms used in this report.

Chapter 1

Acknowledgements

First and foremost I would like to thank my two advisers Professor Gerhard Kristensson and Doctor Jonas Fridén for making this project possible. Their guidance, insight and technical expertise has been invaluable. I would like to thank Doctoral students Iman Vakili, Doruk Tayli and Zachary Miers for providing simulation models, articles and advice. I would like to thank Professor Mats Gustafsson for his enthusiasm for the project, ideas and advice. Many thanks to Professor Anders Karlsson for taking the time to be the Examiner of this work. I would like to thank Jakob Helander for sharing an office with me, getting me through the ups and downs of writing a thesis. Last, but not least, I would like to thank Ella Eriksson for her constant support.

Chapter 2
Introduction

This thesis is a comparison between the antenna properties known as the phase and radiation center. First, we must define the two quantities. The phase center's definition is notoriously vague, the Institute of Electrical and Electronics Engineers (IEEE) standard [1] reads:

> "**2.270 phase center.** The location of a point associated with an antenna such that, if it is taken as the center of a sphere whose radius extends into the far-field, the phase of a given field component over the surface of the radiation sphere is essentially constant, at least over that portion of the surface where the radiation is significant."

This means that the phase center is the point from where the radiation of an antenna seem to originate. For an ideal case, regarding the radiation with the phase center as its origin, would yield a completely constant phase function for the radiation. In reality this is seldom true, rather the phase center is the point which minimizes the phase function. The definition also states that to qualify as a phase center the point has to minimize the part of the phase function which corresponds to high amplitude radiation.

The radiation center is defined in [5]:

> "**Radiation center.** The unique point associated with an antenna such that, if taken as the origin of the far field, the phase variations of the vector far field over the entire radiation sphere are minimized, in the sense of minimized angular momentum."

The angular momentum is a cost function for the phase, minimizing it also minimizes the phase function. However, rather than minimizing the actual phase function, minimizing the angular momentum will minimize the phase depending on the amplitude of the corresponding radiation. As such the angular momentum can be seen as a natural cost function. In Fridén's and Kristensson's article [5] the radiation center was proposed as a substitute for the phase center. In this thesis we aim to prove that the radiation center is not only a replacement for the phase center but also an improvement of the concept.

Previously in [5] the radiation center has been calculated with experimental data. The problem with experimental data is that the actual position of the antenna is seldom documented. This poses a problem when using such data for

radiation center calculations as we are often calculating small displacements along the antenna structure. Hence, in this thesis the antennas will be simulated so we can be sure of their exact position.

Chapter 3
Methodology

The question this thesis aims to answer is if the radiation center is a valid replacement for the phase center as the origin of radiation for antennas. This will be investigated by simulating a number of canonical antennas and calculating the corresponding phase and radiation centers. We will investigate how the radiation and phase center moves under variation of frequency. The merits of the radiation center will be judged by how well it follows previously predicted phase center behaviour. The minimized phase function will also be investigated in order to compare how well the radiation and phase center minimize the phase.

Chapter 4
Theory

The method for calculating the radiation center in this thesis is the same as in [5]. Here follows a review of that theory, but also a derivation of the far-field. Fridén's and Kristensson's method relies on extracting information from the far-field, thus this thesis aims at providing the background needed to understand the origin of this information. We will also briefly touch upon previous methods for calculating the phase center in order to provide material for further discussion.

4.1 Far-field

The far-field is defined as [1]:

> "**2.143** far-field region. That region of the field of an antenna where the angular field distribution is essentially independent of the distance from a specified point in the antenna region."

In other words the far-field of an antenna is the part of its radiated field which is conserved under propagation. Expressed mathematically the far-field decays as $1/r$, where r is the distance from the antenna. However, the energy of the far-field does not decay at all, which can be seen by regarding the total energy per unit area which is proportional to $1/r^2$. The total area of the sphere encompassing the antenna is proportional to r^2. This means that the energy passing through that sphere is constant; the energy of the far-field propagates indefinitely.

The far-field region begins at a distance from the antenna known as the *Fraunhofer distance* which is defined as $2D^2/\lambda$ [8], where D is the largest dimension of the antenna and λ the wavelength; this is only valid if D is large compared to the wavelength. When deriving the Fraunhofer distance the antenna is seen as two point charges separated a distance D from each other. The distance from these sources where the phase error is less than $\pi/8$ is the Fraunhofer distance. Thus the far-field is the region where the phase error in such a configuration is less than $\pi/8$. The value $\pi/8$ is not a fundamental figure derived from first principles, but a value agreed upon giving acceptable measurement results [3].

4.1.1 Deriving the far-field

In this section the relation between the current density and the radiated field is sought. The equations describing the interaction between electric and magnetic fields, Maxwell's equations, is a good place to start. Here the fields are assumed to be time harmonic, with the time convention $e^{\mathrm{j}\omega t}$, thus enabling the use of the time harmonic Maxwell equations,

$$\nabla \cdot \boldsymbol{D} = \rho, \tag{4.1.1}$$
$$\nabla \times \boldsymbol{H} = \boldsymbol{J} + \mathrm{j}\omega \boldsymbol{D}, \tag{4.1.2}$$
$$\nabla \times \boldsymbol{E} = -\mathrm{j}\omega \boldsymbol{B}, \tag{4.1.3}$$
$$\nabla \cdot \boldsymbol{B} = 0, \tag{4.1.4}$$

where $\boldsymbol{D}$ is the electric flux density, $\boldsymbol{H}$ is the magnetic field strength, $\boldsymbol{E}$ is the electric field strength, $\boldsymbol{B}$ is the magnetic flux density, ρ is the charge density, and $\boldsymbol{J}$ is the current density. Gauss' law for magnetism (4.1.4) states that the magnetic flux density $\boldsymbol{B}$ has no divergence. This implies the existence of a vector potential $\boldsymbol{A}$ through the lack of divergence of the curl ($\nabla \cdot (\nabla \times \boldsymbol{A}) = 0$) such that $\boldsymbol{B} = \nabla \times \boldsymbol{A}$. If this expression for $\boldsymbol{B}$ is inserted into Faraday's law of induction (4.1.3) the following relation is found,

$$\nabla \times \boldsymbol{E} = -\mathrm{j}\omega \nabla \times \boldsymbol{A} \Leftrightarrow \nabla \times (\boldsymbol{E} + \mathrm{j}\omega \boldsymbol{A}) = 0. \tag{4.1.5}$$

Because the rotation of the expression (4.1.5) is zero, it corresponds to an irrotational field. This implies the existence of a scalar potential ϕ, since the gradient of a scalar potential has no curl ($\nabla \times (\nabla \phi) = 0$),

$$\boldsymbol{E} = -\nabla \phi - \mathrm{j}\omega \boldsymbol{A}. \tag{4.1.6}$$

These potentials are not uniquely defined, as their origin is based on curls and divergences, some changes can be applied without altering the $\boldsymbol{B}$ or $\boldsymbol{E}$ fields. By using the same trick as above, the gradient of an arbitrary scalar function can be added to $\boldsymbol{A}$ without affecting the evaluation of the $\boldsymbol{B}$ field. However as seen in Equation (4.1.6) the $\boldsymbol{E}$ field does not contain a curl and thus similar modifications have to be made to ϕ to compensate. These alterations are called *gauge transforms* and this freedom is known as the *gauge invariance* of the Maxwell equations,

$$\boldsymbol{A}' = \boldsymbol{A} + \nabla f,$$
$$\phi' = \phi - \mathrm{j}\omega f.$$

Gauge invariance means that the $\boldsymbol{A}$ and ϕ potentials can always be chosen to satisfy the *Lorenz condition* (4.1.7), as they can be transformed to do so,

$$\nabla \cdot \boldsymbol{A} + \frac{\mathrm{j}\omega}{c^2}\phi = 0. \tag{4.1.7}$$

Now we utilize the remaining two Maxwell equations, Gauss's law (4.1.1) and Ampere's circuital law (4.1.2). Using the *constitutive relations* $\boldsymbol{D} = \epsilon \boldsymbol{E}$, $\boldsymbol{B} = \mu \boldsymbol{H}$ they become,

$$\begin{cases} \nabla \cdot \boldsymbol{E} = \dfrac{\rho}{\epsilon}, \\ \nabla \times \boldsymbol{B} = \mu \boldsymbol{J} + \dfrac{\mathrm{j}\omega}{c^2}\boldsymbol{E}, \end{cases} \tag{4.1.8}$$

where μ is the permeability and ϵ is the permittivity which are assumed constant. By expanding equations (4.1.8) with the Lorenz condition (4.1.7) and the potential dependence of the $\boldsymbol{E}$ field (4.1.6) as well as the decomposition of the Laplace operator [7], $\nabla^2\boldsymbol{A} = \nabla(\nabla\cdot\boldsymbol{A}) - \nabla\times(\nabla\times\boldsymbol{A})$, they take on the following form,

$$\begin{cases} k^2\phi + \nabla^2\phi = -\dfrac{1}{\epsilon}\rho, \\ k^2\boldsymbol{A} + \nabla^2\boldsymbol{A} = -\mu\boldsymbol{J}, \end{cases} \tag{4.1.9}$$

where k is the *wave number* defined as $k = 2\pi/\lambda$. Equations (4.1.9) are known as the *inhomogeneous Helmholtz wave equations* and the solution to these are known in terms of the *Green function* $G(\boldsymbol{r})$ [11].

$$\begin{aligned} \phi(\boldsymbol{r}) &= \frac{1}{\epsilon}\int_V \rho(\boldsymbol{r}')G(\boldsymbol{r}-\boldsymbol{r}')\,\mathrm{dV}' = \frac{1}{\epsilon}\int_V \frac{\rho(\boldsymbol{r}')\mathrm{e}^{-\mathrm{j}k|\boldsymbol{r}-\boldsymbol{r}'|}}{4\pi|\boldsymbol{r}-\boldsymbol{r}'|}\,\mathrm{dV}' \\ \boldsymbol{A}(\boldsymbol{r}) &= \mu\int_V \boldsymbol{J}(\boldsymbol{r}')G(\boldsymbol{r}-\boldsymbol{r}')\,\mathrm{dV}' = \mu\int_V \frac{\boldsymbol{J}(\boldsymbol{r}')\mathrm{e}^{-\mathrm{j}k|\boldsymbol{r}-\boldsymbol{r}'|}}{4\pi|\boldsymbol{r}-\boldsymbol{r}'|}\,\mathrm{dV}' \end{aligned} \tag{4.1.10}$$

These expressions are exact and valid everywhere in space provided all currents and charges are known in all space. However, as the far-field is sought a simple condition can be applied to restrict the solutions to the far-field region. The far-field is defined as a region far away from the radiating structure, as such the distance from the object is much larger than the displacement of its parts, $\boldsymbol{r} >> \boldsymbol{r}'$,

$$|\boldsymbol{r}-\boldsymbol{r}'| = \sqrt{(\boldsymbol{r}-\boldsymbol{r}')\cdot(\boldsymbol{r}-\boldsymbol{r}')} = \sqrt{r^2 - 2\boldsymbol{r}\cdot\boldsymbol{r}' + r'^2}, \tag{4.1.11}$$

$$= r\sqrt{1 - 2\hat{\boldsymbol{r}}\cdot\boldsymbol{r}'/r + (r'/r)^2} \approx r - \hat{\boldsymbol{r}}\cdot\boldsymbol{r}'. \tag{4.1.12}$$

The potentials from Equation (4.1.10) can then be written as,

$$\begin{aligned} \phi(\boldsymbol{r}) &\approx \frac{\mathrm{e}^{-\mathrm{j}kr}}{4\pi\epsilon r}\int_V \rho(\boldsymbol{r}')\mathrm{e}^{\mathrm{j}k\boldsymbol{r}'\cdot\hat{\boldsymbol{r}}}\,\mathrm{dV}', \\ \boldsymbol{A}(\boldsymbol{r}) &\approx \frac{\mathrm{e}^{-\mathrm{j}kr}\mu}{4\pi r}\int_V \boldsymbol{J}(\boldsymbol{r}')\mathrm{e}^{\mathrm{j}k\boldsymbol{r}'\cdot\hat{\boldsymbol{r}}}\mathrm{dV}', \end{aligned} \tag{4.1.13}$$

in the far-field. As a relation between the radiated field and the current density $\boldsymbol{J}$ is sought we would like to eliminate the charge density ρ. This can be done by considering the divergence of Ampere's circuital law (4.1.2),

$$\nabla\cdot\boldsymbol{J} + \mathrm{j}\omega\rho = 0. \tag{4.1.14}$$

This relation is known as *the conservation of charge*. Now we can rewrite Equation (4.1.6) with Equation (4.1.14),

$$\boldsymbol{E}(\boldsymbol{r}) \approx -\mathrm{j}\omega\frac{\mathrm{e}^{-\mathrm{j}kr}}{4\pi r}\int_V \left[\mu\boldsymbol{J}(\boldsymbol{r}') - \frac{1}{\epsilon}\nabla(\nabla\cdot\boldsymbol{J}(\boldsymbol{r}'))\right]\mathrm{e}^{\mathrm{j}k\boldsymbol{r}'\cdot\hat{\boldsymbol{r}}}\mathrm{dV}'. \tag{4.1.15}$$

To simplify notation, the radiation vector $\boldsymbol{K}(\hat{\boldsymbol{r}})$ is introduced,

$$\boldsymbol{K}(\hat{\boldsymbol{r}}) = \frac{-\mathrm{j}k^2\eta}{4\pi}\int_V \mathrm{e}^{\mathrm{j}k\boldsymbol{r}'\cdot\hat{\boldsymbol{r}}}\boldsymbol{J}(\boldsymbol{r}')\,\mathrm{dV}', \tag{4.1.16}$$

where η is known as the free space impedance and is defined as $\eta = \sqrt{\mu/\epsilon}$. Notice that the radiation vector is a simple Fourier transform of the current $\boldsymbol{J}$. Now Equation (4.1.15) can be written in the following way,

$$\boldsymbol{E}(\boldsymbol{r}) \approx \left[\mathbf{I} + \frac{1}{k^2}\nabla\nabla\right] \cdot \left(\frac{\mathrm{e}^{-\mathrm{j}kr}}{kr}\boldsymbol{K}(\hat{\boldsymbol{r}})\right). \tag{4.1.17}$$

When we regard the effect of the first of the divergence operators in (4.1.17) we get,

$$\nabla \cdot \left[\frac{\mathrm{e}^{-\mathrm{j}kr}}{kr}\boldsymbol{K}(\hat{\boldsymbol{r}})\right] = \frac{\mathrm{e}^{-\mathrm{j}kr}}{kr}\nabla \cdot \boldsymbol{K}(\hat{\boldsymbol{r}}) + \boldsymbol{K}(\hat{\boldsymbol{r}}) \cdot \nabla\left(\frac{\mathrm{e}^{-\mathrm{j}kr}}{kr}\right). \tag{4.1.18}$$

$\boldsymbol{K}(\hat{\boldsymbol{r}})$ depends exclusively on the direction $\hat{\boldsymbol{r}}$ which can be described by the θ and ϕ angles and does not depend on the distance r. Thus the divergence of $\boldsymbol{K}(\hat{\boldsymbol{r}})$ will be [2],

$$\nabla \cdot \boldsymbol{K}(\hat{\boldsymbol{r}}) = \frac{1}{r\sin\theta}\frac{\partial}{\partial\theta}(\sin\theta K_\theta) + \frac{1}{r\sin\theta}\frac{\partial}{\partial\phi}(K_\phi),$$

which decreases as $1/r$. Because the divergence of $\boldsymbol{K}(\hat{\boldsymbol{r}})$ is multiplied with $1/kr$ in (4.1.18) the total expression will decrease as $1/r^2$. Thus that term will be negligible in the far-field where r is large,

$$\begin{aligned}\frac{1}{k}\nabla \cdot \left[\frac{\mathrm{e}^{-\mathrm{j}kr}}{kr}\boldsymbol{K}(\hat{\boldsymbol{r}})\right] &= \frac{1}{k}\boldsymbol{K}(\hat{\boldsymbol{r}}) \cdot \nabla\left(\frac{\mathrm{e}^{-\mathrm{j}kr}}{kr}\right)(1 + O((kr)^{-1})) \\ &= -\mathrm{j}\hat{\boldsymbol{r}} \cdot \boldsymbol{K}(\hat{\boldsymbol{r}})\frac{\mathrm{e}^{-\mathrm{j}kr}}{kr}(1 + O((kr)^{-1})).\end{aligned}$$

The same principle can be applied to the second divergence operator resulting in the following equation,

$$\frac{1}{k^2}\nabla\left\{\nabla \cdot \left[\frac{\mathrm{e}^{-\mathrm{j}kr}}{kr}\boldsymbol{K}(\hat{\boldsymbol{r}})\right]\right\} = -\hat{\boldsymbol{r}}(\hat{\boldsymbol{r}} \cdot \boldsymbol{K}(\hat{\boldsymbol{r}}))\frac{\mathrm{e}^{-\mathrm{j}kr}}{kr}(1 + O((kr)^{-1})). \tag{4.1.19}$$

Finally (4.1.19) can be put back into Equation (4.1.17) to get the main contribution in the far-field,

$$\boldsymbol{E}(\boldsymbol{r}) = [\boldsymbol{K}(\hat{\boldsymbol{r}}) - \hat{\boldsymbol{r}}(\hat{\boldsymbol{r}} \cdot \boldsymbol{K}(\hat{\boldsymbol{r}}))]\frac{\mathrm{e}^{-\mathrm{j}kr}}{kr} = \hat{\boldsymbol{r}} \times (\boldsymbol{K}(\hat{\boldsymbol{r}}) \times \hat{\boldsymbol{r}})\frac{\mathrm{e}^{-\mathrm{j}kr}}{kr}.$$

This is the electrical far-field which ends up as a simple projection of the Fourier transform of the current $\boldsymbol{J}$. The expression is further simplified by defining the *far-field amplitude* $\boldsymbol{F}(\hat{\boldsymbol{r}})$ [13] as,

$$\boldsymbol{F}(\hat{\boldsymbol{r}}) = \hat{\boldsymbol{r}} \times (\boldsymbol{K}(\hat{\boldsymbol{r}}) \times \hat{\boldsymbol{r}}). \tag{4.1.20}$$

The far-field amplitude can also be written in terms of the electric field, this definition will form the basis for most of the analysis later on,

$$\boldsymbol{F}(\hat{\boldsymbol{r}}) = \lim_{r\to\infty} kr\mathrm{e}^{\mathrm{j}kr}\boldsymbol{E}(\boldsymbol{r}), \tag{4.1.21}$$

in this definition the far-field amplitude and the electric field share the same units, V/m.

4.2 Finding the radiation center

This section follows to a large extent Fridén's and Kristensson's paper *Calculation of antenna radiation center using angular momentum* [5]. The main reason for this repetition is that Fridén's and Kristensson's theory forms a central part of the analysis presented in this thesis, and for the convenience to the the reader, the details are worth repeating.

The method presented in Fridén's and Kristensson's paper revolves around using the quantum mechanical angular momentum operator as a cost function. By minimizing this cost function, an unique point is found and defined as the radiation center. To do this, parallels are drawn between the far-field and quantum mechanical states. In quantum mechanics unmeasured states are seen as superpositions of fundamental states, e.g. spin up and spin down. To formulate a theory for the quantum angular momentum operator acting on the far-field, we have to express the far-field in a way that is consistent with the quantum mechanical state. The Spherical Wave Expansion (SWE) is chosen to fulfill this role.

Firstly the far-field amplitude, defined in (4.1.21), is normalized as,

$$\iint_{\Omega} \boldsymbol{F}^*(\hat{\boldsymbol{r}}) \cdot \boldsymbol{F}(\hat{\boldsymbol{r}}) \, \mathrm{d}\Omega = 1, \tag{4.2.1}$$

where Ω is the unit sphere and $\mathrm{d}\Omega$ is the measure of the unit sphere. The SWE of the far-field amplitude is a sum of *vector spherical harmonics* $\boldsymbol{A}_{\tau lm}$, defined in appendix A,

$$\boldsymbol{F}(\hat{\boldsymbol{r}}) = \sum_{\tau=1}^{2} \sum_{l=1}^{\infty} \sum_{m=-l}^{l} a_{\tau lm} \boldsymbol{A}_{\tau lm}(\hat{\boldsymbol{r}}) = \sum_{\tau lm} a_{\tau lm} \boldsymbol{A}_{\tau lm}(\hat{\boldsymbol{r}}), \tag{4.2.2}$$

where each $\boldsymbol{A}_{\tau lm}$ represent a mode weighted by the mode amplitude $a_{\tau lm}$. These mode amplitudes are obtained with the use of the orthogonality of the vector spherical harmonics,

$$a_{\tau lm} = \iint_{\Omega} \boldsymbol{A}^*_{\tau lm} \cdot \boldsymbol{F}(\hat{\boldsymbol{r}}) \, \mathrm{d}\Omega, \tag{4.2.3}$$

and their normalization is found with the help of (4.2.1)

$$\sum_{\tau lm} |a_{\tau lm}|^2 = 1.$$

The vector spherical harmonics are eigenstates which operators act upon, where the indices l and m correspond to the quantum state indices with the same name, l is the length of the state and m is the projection in a certain direction. The quantum mechanical angular momentum is defined as

$$\begin{cases} \boldsymbol{L}^2 |l, m\rangle = l(l+1)|l, m\rangle, \\ L_z^2 |l, m\rangle = m^2 |l, m\rangle. \end{cases}$$

Where $|l, m\rangle$ is the quantum state, $\boldsymbol{L}$ is the quantum angular momentum operator and $\hbar = 1$ [21]. In analogy with the quantum mechanical angular momentum, for

the far-field we adopt

$$\begin{cases} L^2 = \sum_{\tau lm} l(l+1)|a_{\tau lm}|^2, \\ L_z^2 = \sum_{\tau lm} m^2|a_{\tau lm}|^2. \end{cases} \tag{4.2.4}$$

These are the cost functions that will be minimized to find the radiation center. By translating the origin of the far-field, the mode coefficients $a_{\tau lm}$ vary by (4.2.3) and thus in turn the angular momentum. In order to calculate the minimum we need to know how the far-field behaves under operations such as translation and rotation. Now that an intuitive derivation has been made, a formal argument is given in the following section.

4.3 The Angular momentum operator

In classical mechanics the angular momentum operator is defined as [6],

$$\boldsymbol{L} = \boldsymbol{r} \times \boldsymbol{p}, \tag{4.3.1}$$

where $\boldsymbol{p}$ is the linear momentum. In quantum mechanics the linear momentum is expressed as $-\mathrm{j}\nabla$[1], which leads to the following expression for angular momentum,

$$\mathcal{L} = -\mathrm{j}(\boldsymbol{r} \times \nabla). \tag{4.3.2}$$

The operators used to calculate the intended cost function L^2 are

$$\begin{cases} \mathcal{L}^2 = \mathcal{L} \cdot \mathcal{L} = -(\boldsymbol{r} \times \nabla) \cdot (\boldsymbol{r} \times \nabla) = -\nabla_\Omega^2, \\ \mathcal{L}_n = \hat{\boldsymbol{n}} \cdot \mathcal{L}, \\ \mathcal{L}_n^2 = (\hat{\boldsymbol{n}} \cdot \mathcal{L})(\hat{\boldsymbol{n}} \cdot \mathcal{L}), \end{cases} \tag{4.3.3}$$

where ∇_Ω is the angular part of the Laplace operator defined in (**??**). For the spherical vector waves to be eigenstates to the squared angular momentum operator, and thus be able to fulfill (4.2.4), a projection operator $\mathcal{P}_\Omega$ has to be added to the operator. The relations then become, see [16, pp. 1865] and Appendix A,

$$\begin{cases} \mathcal{P}_\Omega \mathcal{L}^2 \boldsymbol{A}_{\tau lm} = l(l+1)\boldsymbol{A}_{\tau lm}, \\ \mathcal{L}_z(\hat{\boldsymbol{\theta}} \cdot \boldsymbol{A}_{\tau lm}) = m(\hat{\boldsymbol{\theta}} \cdot \boldsymbol{A}_{\tau lm}), \\ \mathcal{L}_z(\hat{\boldsymbol{\phi}} \cdot \boldsymbol{A}_{\tau lm}) = m(\hat{\boldsymbol{\phi}} \cdot \boldsymbol{A}_{\tau lm}). \end{cases}$$

Now it is easily seen that the intuitive relation (4.2.4) is in fact correct. The quantum mechanical angular momentum operator can be applied to the far-field with impunity and is a good choice of cost function.

[1] Formally, the imaginary unit j in the quantum mechanical definition of the linear momentum has a different origin compared to the imaginary unit j used in the rest of the thesis, which denotes the adopted time convention. There is no risk of these two different imaginary units interacting, since all analysis is carried out with squared operators.

4.4 Properties of angular momentum

In classical mechanics angular momentum has a couple of properties which are relevant to our analysis:

1. $|\boldsymbol{L}|$ is conserved under rotation.

2. L^2 has the quadratic form under translations with the vector $\boldsymbol{d}$:
   $\boldsymbol{L}\cdot\boldsymbol{L} \Rightarrow \boldsymbol{L}\cdot\boldsymbol{L} - 2\boldsymbol{d}\cdot(\boldsymbol{p}\times\boldsymbol{L}) + \boldsymbol{d}\cdot(\mathbf{I}|\boldsymbol{p}|^2 - \boldsymbol{pp})\cdot\boldsymbol{d}$

These properties hold for the quadratic angular momentum L^2 used in this thesis, which will be proven in the following sections.

4.4.1 Conservation under rotation

$\mathcal{R}(\alpha,\beta,\gamma)$ is the active Euler rotation operator defined in appendix E, which consists of z and y rotations. For vector spherical harmonics $\boldsymbol{A}_{\tau lm}$ y-rotations shifts the m index and z-rotations only shift the phase of the mode amplitudes $a_{\tau lm}$[8]. L^2 is a squared quantity and is thus invariant under z-rotations. To see that y-rotations do not affect L^2, we regard an y only rotation operator acting upon $\boldsymbol{A}_{\tau lm}$,

$$\mathcal{R}(0,\beta,0)\boldsymbol{A}_{\tau lm}(\hat{\boldsymbol{r}}) = \sum_{m'=-l}^{l} d^l_{mm'}(\beta)\boldsymbol{A}_{\tau lm'}(\hat{\boldsymbol{r}}), \tag{4.4.1}$$

where the real coefficients $d^l_{mm'}(\beta)$ satisfy

$$\sum_{m''=-l}^{l} d^l_{m''m}(\beta)d^l_{m''m'}(\beta) = \delta_{mm'}.$$

By (4.4.1) the mode coefficients transform as

$$a_{\tau lm}(\beta) = \sum_{m''=-l}^{l} d^l_{mm'}(\beta)a_{\tau lm'}.$$

The squared value can then be calculated

$$\begin{aligned}
&\sum_m |a_{\tau lm}|^2 = \\
&\sum_m \sum_{m'} \sum_{m''} d^l_{mm'}(\beta)d^l_{mm''}(\beta)a^*_{\tau lm'}a_{\tau lm''} = \\
&\sum_{m'} \sum_{m''} \delta_{m'm''}a^*_{\tau lm'}a_{\tau lm''} = \sum_{m'} |a_{\tau lm'}|^2,
\end{aligned}$$

where all summations are taken from $-l$ to l. Thus L^2 does not change under rotations [9].

4.4.2 Translation

To analyze the consequence of translating the far-field for the squared angular momentum we must first derive the mathematical expression for such a translation. Let $\boldsymbol{d}$ be the distance translated, $\boldsymbol{r}'$ the distance from the new origin to a point in the far-field and $\boldsymbol{r}$ the distance from the original origin. These can be related as

$$\boldsymbol{r} = \boldsymbol{d} + \boldsymbol{r}'.$$

The magnitude of the distance becomes, with the help of (4.1.11),

$$r = |\boldsymbol{r} + \boldsymbol{d}| \approx r' + \hat{\boldsymbol{r}} \cdot \boldsymbol{d}, \text{as } r, r' \to \infty.$$

At large distances the directions $\hat{\boldsymbol{r}}$ and $\hat{\boldsymbol{r}}'$ become the same direction because,

$$\hat{\boldsymbol{r}} = \lim_{r\to\infty} \frac{\boldsymbol{r}}{r} = \lim_{r\to\infty} \frac{\boldsymbol{d}+\boldsymbol{r}'}{|\boldsymbol{d}+\boldsymbol{r}'|} = \lim_{r\to\infty} \frac{\boldsymbol{d}/r' + \hat{\boldsymbol{r}}'}{|\boldsymbol{d}/r' + \hat{\boldsymbol{r}}'|} = \lim_{r'\to\infty} \frac{\boldsymbol{d}/r' + \hat{\boldsymbol{r}}'}{|\boldsymbol{d}/r' + \hat{\boldsymbol{r}}'|} = \hat{\boldsymbol{r}}'.$$

Regard the definition of the far-field amplitude (4.1.21) for the translated field,

$$\boldsymbol{F}'(\hat{\boldsymbol{r}}) = \boldsymbol{F}'(\hat{\boldsymbol{r}}') = \lim_{r'\to\infty} kr' \mathrm{e}^{\mathrm{j}kr} \boldsymbol{E}(\boldsymbol{r}') = \lim_{r\to\infty} k(r - \hat{\boldsymbol{r}}\cdot\boldsymbol{d}) \mathrm{e}^{\mathrm{j}k(r-\hat{\boldsymbol{r}}\cdot\boldsymbol{d})} \boldsymbol{E}(\boldsymbol{r}-\boldsymbol{d}).$$

As $|\boldsymbol{r}|$ is much greater than $|\boldsymbol{d}|$ we get,

$$\boldsymbol{F}'(\hat{\boldsymbol{r}}) = \lim_{r\to\infty} kr \mathrm{e}^{\mathrm{j}k(r-\hat{\boldsymbol{r}}\cdot\boldsymbol{d})} \boldsymbol{E}(\boldsymbol{r}-\boldsymbol{d}) = \mathrm{e}^{-\mathrm{j}k\hat{\boldsymbol{r}}\cdot\boldsymbol{d}} \lim_{r\to\infty} r\mathrm{e}^{\mathrm{j}kr} \boldsymbol{E}(\boldsymbol{r}).$$

Which can be written as a scalar term multiplied to the original far-field,

$$\boldsymbol{F}'(\hat{\boldsymbol{r}}) = \mathrm{e}^{-\mathrm{j}k\hat{\boldsymbol{r}}\cdot\boldsymbol{d}} \boldsymbol{F}(\hat{\boldsymbol{r}}). \tag{4.4.2}$$

With the mathematical expression for the translated far-field in (4.4.2) the translated squared quantum angular momentum can be written in the following form, see Appendix D,

$$L^2(\boldsymbol{d}) = a_0 + 2k\boldsymbol{a}_1 \cdot \boldsymbol{d} + k^2 \boldsymbol{d} \cdot \mathbf{A}_2 \cdot \boldsymbol{d}, \tag{4.4.3}$$

where a_0 is a real number, $\boldsymbol{a}_1$ is a real-valued vector, and $\boldsymbol{A}_2$ is a positive definite dyadic, see Appendix D,

$$\begin{cases} a_0 = L^2(\boldsymbol{F}(\hat{\boldsymbol{r}}), 0) = \iint_\Omega \boldsymbol{F}^* \cdot \mathcal{L}^2 \boldsymbol{F} \,\mathrm{d}\Omega, \\ \boldsymbol{a}_1 = \iint_\Omega \mathrm{Im}[F_\theta \nabla_\Omega F_\theta^* + F_\phi \nabla_\Omega F_\phi^*] \,\mathrm{d}\Omega - 2 \iint_\Omega \cot\theta \ \mathrm{Im}(F_\theta F_\phi^*) \hat{\boldsymbol{\phi}} \,\mathrm{d}\Omega \\ \mathbf{A}_2 = \iint_\Omega (\boldsymbol{F}^* \cdot \boldsymbol{F})[\hat{\boldsymbol{\theta}}\hat{\boldsymbol{\theta}} + \hat{\boldsymbol{\phi}}\hat{\boldsymbol{\phi}}] \,\mathrm{d}\Omega. \end{cases} \tag{4.4.4}$$

Equation (4.4.3) is formally equivalent to the translated classical angular momentum given in Section 4.4, and thus behaves in the same way.

4.5 Calculating the minimum

To minimize the squared angular momentum we seek the translation vector $\boldsymbol{d}_{min}$ which corresponds to the minimum. In section 4.4.2 we derived the analytical expression for translation of the far-field (4.4.3). This expression is a quadratic form where $\mathbf{A}_2$ is a positive definite dyadic, see appendix D. Hence L^2 forms a parabola curve with regards to the translated distance that has a strict global minimum. Thus this minimum can easily be calculated with elementary matrix algebra,

$$\boldsymbol{d}_{min} = -\frac{1}{k}\mathbf{A}_2^{-1} \cdot \boldsymbol{a}_1. \tag{4.5.1}$$

4.6 Phase center

4.6.1 E- and H-plane

When we are discussing the phase center we will often refer to the E- and H-plane. These planes simply denote two orthogonal planes which help us understand which direction we are talking about in relation to the antenna. They are defined for linearly polarized antennas, where the E-plane corresponds to the electric field in the vertical direction and the H-plane to the magnetic field in the horizontal direction.

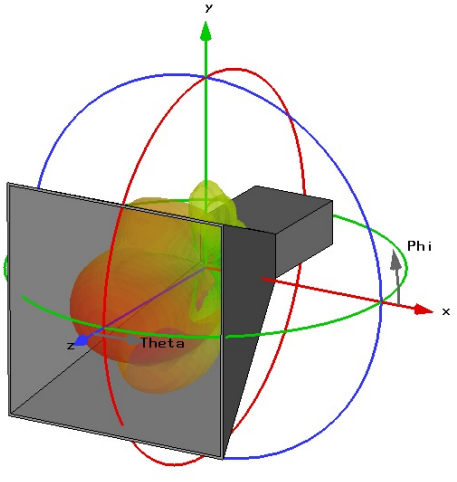

Figure 4.1: Visualization of a horn antenna in CST.

All antennas simulated in this thesis have been oriented to radiate in the z direction as shown in figure 4.1. The E-plane is then defined as when $\phi = 90^{\text{o}}$ and the H-plane as $\phi = 0^{\text{o}}$.

4.6.2 Standard phase center calculation

The method used by CST to calculate the phase center is known as the *Least-squares fit* method. This method tries to match the phase function of the antenna to a flat phase. The phase is calculated for a variety of locations of the antenna, the deviation from the ideal phase function is then calculated for each of these. Finally the least deviation is found by minimizing the difference in a least-square sense.

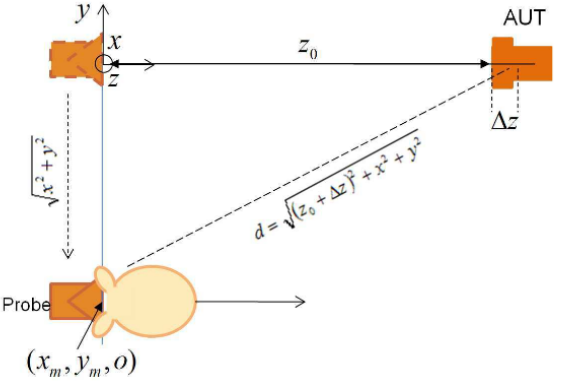

Figure 4.2: Visualization of the Least-squares method curtesy of Pablo Padilla et. al. [20]. In this figure the probe is moved around the AUT to measure all the points of the phase function. z_0 is the fixed distance between the far-field and the AUT.

If the scheme in Figure 4.2 is followed, the equation to calculate the minimum then becomes [20, eq. 1],

$$S(\Delta z) = \min \sum_n \sum_m (\phi_{meas.}(x_n, y_m, z_0) - \phi_{th}(x_n, y_m, z_0 + \Delta z))^2, \qquad (4.6.1)$$

where $\phi_{meas.}$ is the measured phase, ϕ_{th} is the ideal case, x_n and y_m describe the far-field points, z_0 refers to the fixed distance and Δz to the phase center. This calculation is done in one plane at a time as it is often not possible to define a unique 3 dimensional phase center with this method. CST's *Bore sight* method solves this problem by calculating the phase center in this manner in 3 different planes and then taking the average as the total phase center. In this kind of method we need to decide which part of the phase function we are interested in. This is most commonly done by letting the user decide an angular interval around the main radiation direction. Only points within this interval are considered when calculating the phase center.

4.6.3 Analytical phase center calculation for horn antennas

There are other methods of phase center calculation that differ from the one presented in section 4.6.2. These methods are often based around using features of the antenna to enable analytical calculation of the phase center, as such these methods are unique to each type of antenna. The method presented by Muehldorf[17] defines such a method for horn antennas.

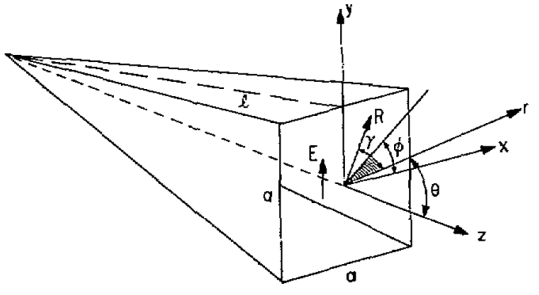

xyz	rectangular coordinate system
$r\theta\phi$	spherical coordinate system
θ	angle between r and z
ϕ	angle between x and projection of r on xy plane
γ	angle between r and R
R	distance from origin to a point in xy plane.

Figure 4.3: Courtesy of Eugen I. Muehldorf [17]

Muehldorf not only calculates the far-field analytically by integrating over the aperture, but also introduces a correction for the phase front to increase accuracy. Instead of letting the phase front coincide with the aperture front, it is approximated as a paraboloid of rotation [17, eq. (1)]

$$\delta = -\frac{x^2 + y^2}{2l} + \frac{a^2}{4l} \tag{4.6.2}$$

where l is the length of the horn, a the width of the aperture and δ the deviation of the phase front from the aperture plane. The phase center is found by selecting a plane with fixed ϕ, and approximating the phase front in a two dimensional curve. This is usually done with $\phi = 0°$ or $90°$ to select the H- or E-plane. The radius of the curvature, ρ, is then calculated close the z-axis in Figure 4.3,

$$\rho = \frac{[r^2 + (r')^2]^{3/2}}{r^2 + 2(r')^2 - rr''},$$

where r is the radial coordinate to the phase front in the spherical cooridantes. The radius of the curvature of the phase function is the quantity which minimizes the phase and thus the phase center. However, the phase center needs to be given in relation to an aspect of the antenna. The phase center Δ is thus defined as the radius of the curvature plus the distance between the aperture and the phase front[17, eq. (7)].

$$\Delta = \rho - r(0) \tag{4.6.3}$$

This relation is very simple in its essence, but the equations describing the phase front and its curvature radius become very complex when calculated explicitly, see [17] for further details. This method is based around the first excitation mode of the horn, as such it can not be used to calculate the phase center for higher frequencies where additional modes are excited.

4.7 Phase center or Radiation center

One difference between the phase and radiation center is how the angular cost function is selected. The radiation center is calculated through translation of the far-field in Equation (4.5.1), in direct consequence of this the radiation center prioritizes the phase of high amplitude radiation. The phase center on the other hand prioritizes the phase from user input. This user input is meant to correspond to the half power beam width of the main radiation lobe of the antenna. When the user selected angular cut corresponds well to the main radiation lobe the phase data minimized is much the same for the radiation and phase center. However, the radiation center calculation takes the rest of the radiation into account as well, such as side lobes and asymmetrical beams. What needs to be evaluated through simulation is whether such extra factors are detrimental or positive in the search for a origin of the radiation.

4.7.1 Effects of angular truncation

The radiation center is normally calculated over the entire sphere, resulting in one unique point. This is different in many phase center calculations which only treat one plane at a time. These methods are thus never able to define any unique center, but rather a phase center for each plane, normally the E- and H-plane. To resolve this issue, algorithms, such as the one used in CST, uses the average position of the phase center in several planes and denote the resulting point the total phase center. However, this only yields accurate results for antennas where the phase centers are close to each other, such as pyramidal horns [14, pp. 8-76]. To be able to compare the radiation and phase center for antennas with very different E- and H-plane phase centers the radiation center has been calculated using vertical and horizontal angular cuts. These cuts correspond to the E- and H-plane.

Chapter 5
Results

Even though the phase center is a vaguely defined antenna parameter, there exist some assumptions and accepted truths on the subject. For some of the most common antennas, such as the horn antenna, there is a general understanding of how the phase center should behave under variation of frequency. For other antennas, such as the dipole, we know the phase center position from symmetry [1]. In order to determine the validity of the radiation center as a substitute for the phase center, these common types of antennas have been simulated and evaluated with the angular momentum method described in Chapter 4. The phase center has also been calculated with the standard methods described in Section 4.6 for comparison. The phase center has been calculated in CST with different angular truncations to see how this affects the phase center in comparison to the radiation center. The radiation center has also been calculated with stricter angular truncations in order to see how well such a calculation matches the phase center in the E- or H-plane. To understand the difference after minimization with the different phase and radiation centers the phase function has been plotted for some of the antennas.

[1] The dipole has rotational symmetry around its axis and under inversion of that axis. The phase and radiation center must obey these symmetries as well. Hence the radiation and phase center must lie in the middle of the antenna.

5.1 Consistency check of simulated results

To be sure that the CST software does not alter information in the far-field which is essential to our calculations, some tests have been run. These tests consist of moving an antenna element off center to see the calculated radiation centers' behaviour under translation of the far-field in CST. If the relation is linear we can safely say that CST does not manipulate the far-field in some unexpected way. These simulations have been carried out in the manner described in Appendix F.2.

5.1.1 Dipole

The Dipole is an elementary antenna consisting of two thin wires which have a total length of $\lambda/2$. Since the dipole is a very simple resonant structure we have a good idea of where its phase center should be. The dipole has an omni-diectional symmetrical radiation pattern for all frequencies. Because of the symmetry in such a radiation pattern, the classical phase center is fixed in the middle of the structure for all frequencies. This is also true for the radiation center [5]. As both theories agree about the phase and radiation centers position the dipole is a good choice to verify our simulation methods.

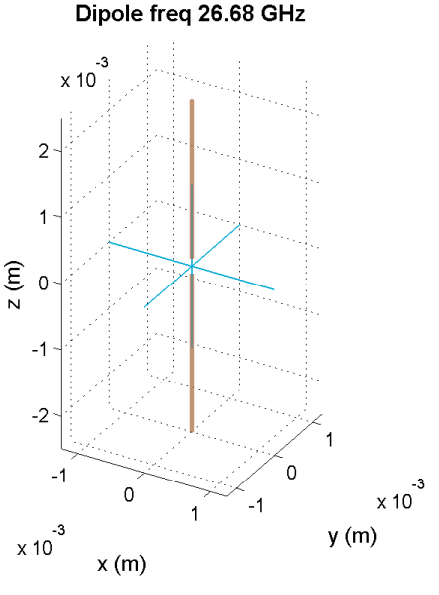

Figure 5.1: Radiation center for a dipole at its resonant frequency.

In Figure 5.1 we see that the radiation center falls in the center of the dipole, as expected. Then we at least know that a simulation of a fixed dipole provides correct results. An important feature of the radiation center is its additive properties [4]. The dipole has thus been translated in CST, as described in Appendix F.2, to verify this property in our simulations.

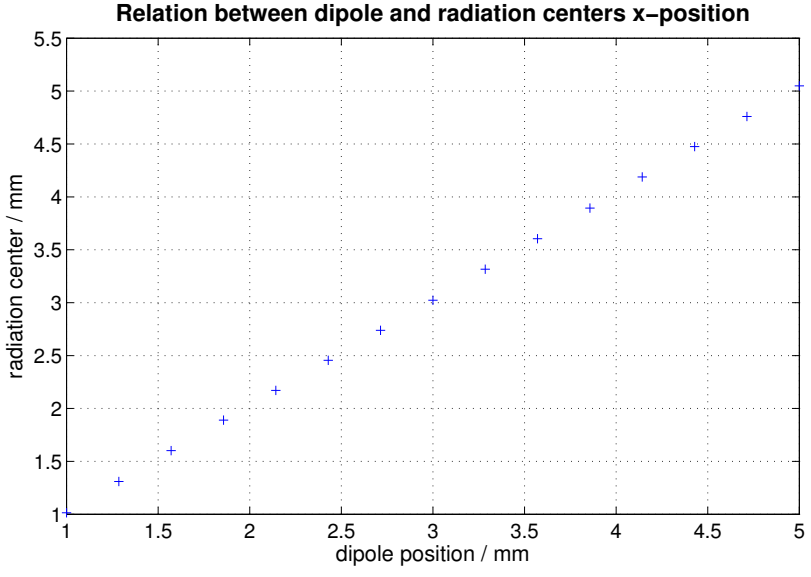

Figure 5.2: The relation of the shifted dipole and its x coordinate is not only linear but also equal as the dipole has been defined around the origin.

In Figure 5.2 we see that the radiation center and the dipole coincide as the dipole is translated away from the origin.

5.1.2 Horn antenna

The antennas simulated in this thesis are not as simple as the dipole. Therefore another antenna was chosen to further verify the additive property of the simulated radiation center. The horn antenna presented here is further investigated in Section 5.2.1.

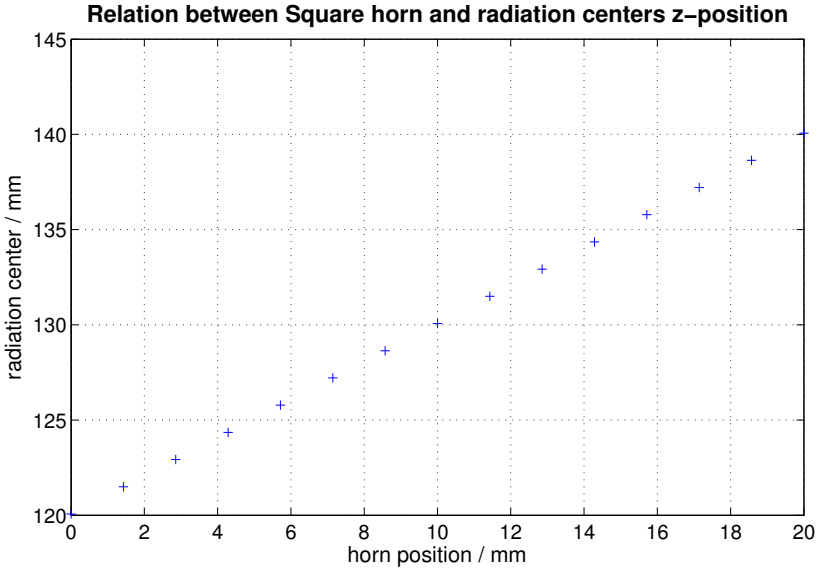

Figure 5.3: The relation between the translation of the horn antenna and its radiation center is linear. As the radiation center is located at the aperture of the horn for this frequency the initial position is large, but the relation between it and the translation is 1:1.

As can be seen for both the dipole and the horn in Figure 5.2 and 5.3 the relation between translation of the far-field in CST and the radiation centers position is linear. Therefore we can conclude that CST provides us with unmodified far-field data which can be trusted to provide sound results.

5.2 Horn antennas

A horn antenna consists of a flaring aperture attached to a waveguide. The horn antenna functions for frequencies above the cut-off frequency of its waveguide. It is commonly used as a broadband antenna as it has relatively high directivity, low voltage standing wave ratio and large bandwidth [12, ch. 14]. Finding the phase center, or radiation center, is also of interest for horn applications such as interferometers or reflector feeds where the electric position of the antenna is very important [17, 14, 24]. In our analysis the horn is interesting to investigate as its phase center should vary with frequency. The phase center is well known for horn antennas and is expected to move from the aperture into the horn as the frequency is increased. The phase center should not progress further into the horn than the apertures imaginary apex [17, 14, ch. 8]. We will characterize our horns by; length; aperture height and width, see H and W in Figure 5.4; as well as imaginary aperture apex. The imaginary aperture apex is the point where the sides of the aperture meet if they are extended into the waveguide, see Figure 5.4

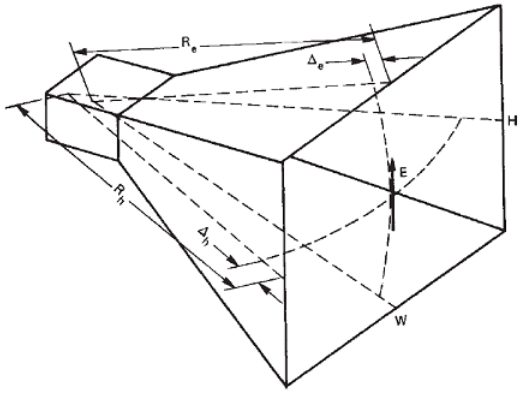

Figure 5.4: Horn geometry courtesy of Thomas A. Milligan [15]. This figure shows the idea of imaginary apexes and the fact that they do not always coincide with each other. Where the distance R_e denotes the distance from the aperture to the imaginary E-plane aperture apex and R_h to the imaginary H-plane aperture apex.

5.2.1 Square horn antenna

The square horn has an aperture with equal width and height. Hence, the aperture's angles of expansion are different for the E- and H-plane, due to the rectangular waveguide. This means that the imaginary aperture apex is different for the two sides, see Figure 5.4. Because of the difference in angle of expansion, there should be a difference in phase center position for E- and H-plane [17].

Square Horn					
Length (mm)		148.6			
Waveguide length (mm)		48			
Aperture height H (mm)		100			
Aperture width W (mm)		100			
		H-plane		**E-plane**	
Waveguide (mm)		35		17.5	
Aperture apex (mm)		-6.2		26.7	
E-plane mode index	m	1	2	0	1
H-plane mode index	n	0	0	1	1
Mode cut-off frequency (GHz)		4.28	8.56	8.56	9.58

Table 5.1: Specification of the simulated square aperture horn antenna. The distances for the aperture apexes are given from the back of waveguide feed.

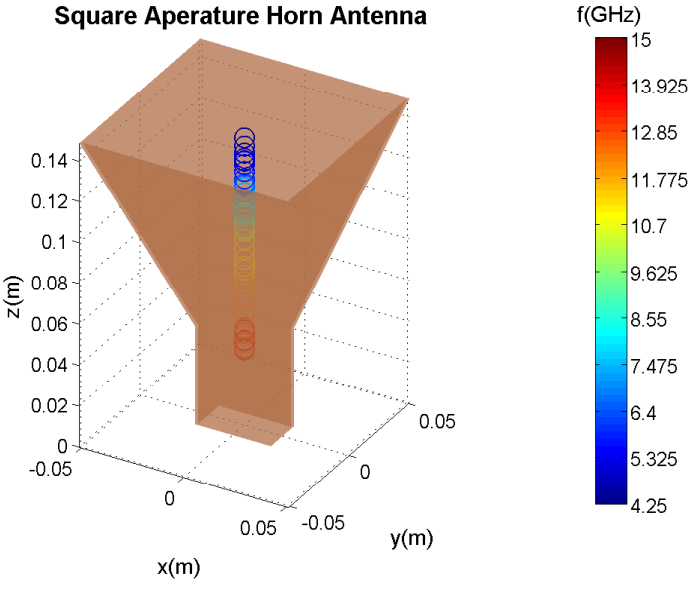

Figure 5.5: Radiation center of a square horn antenna.

In Figure 5.5 we can see that the radiation center conforms to the expected behaviour of the phase center. Starting at the end of the horn at the first lowest simulated frequency the radiation center progresses with no horizontal deviation into the horn. Graphs for the x and y directions are thus not included as the variation in these directions are negligible. Even though we have simulated well beyond the cut-off frequency of the second mode in the feeding waveguide, the radiation center has not passed below any of the imaginary apexes of the aperture found in Table 5.1.

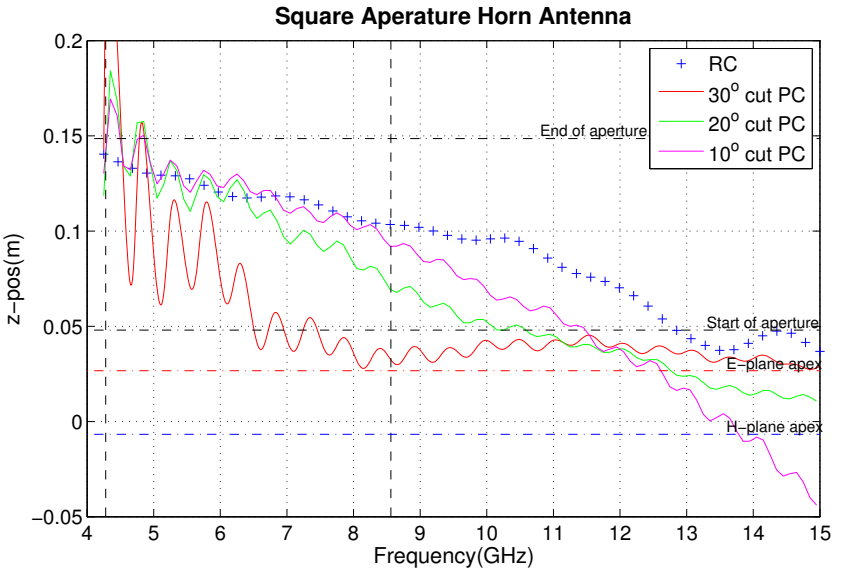

Figure 5.6: A comparison between the radiation center and the phase center for the square aperture horn antenna where the origin is defined at the back of the simulated structure. The two vertical dashed black lines denote the first and second cut-off frequencies of the feeding waveguide. The HPBW varies from 40 degrees for low frequencies to 15 degrees at high frequencies.

If nothing else is specified, the 30 degree cut for the phase center calculation is the standard value used by CST. In Figure 5.6 we see that the phase center based on a 30 degree cut oscillates heavily at low frequencies and quickly drops to a value in the region slightly above the E-plane imaginary aperture apex. The quick drop off is not predicted by analytical theories, see Figure 5.7. If we instead regard the calculations made with narrower cuts, we see that these conform to the expected behaviour. The phase center based on 20 degree cuts drops off gradually, with smaller oscillation, towards the imaginary aperture apex. This is also true for the 10 degree cut phase center, but it drops off through the back of the antenna at high frequencies. When the 10 and 20 degree cuts are regarded in relation to the radiation center, we see that the 10 degree cut follows the radiation center curve more closely for low frequencies. However, the phase center and radiation center curves have approximately the same behaviour for both the 10 and 20 degree phase cuts. Also note that the oscillations present throughout the CST simulation results are much less prominent for the radiation center. Oscillations still exist for the radiation center but they have far less amplitude and a slower variation with frequency.

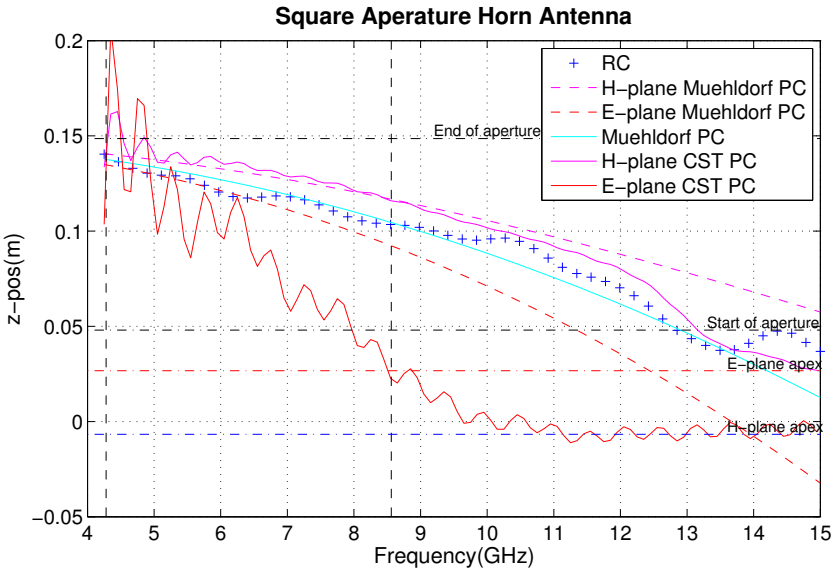

Figure 5.7: A comparison between the radiation center, the phase center calculated theoretically by the Muehldorf method and simulated data from CST. The two vertical dashed black lines denote the first and second cut-off frequencies of the feeding waveguide. Note that the Muehldorf phase center calculations are only based on the first mode.

The Muehldorf phase center has been calculated by taking the average value of the H-plane and E-plane Muehldorf phase centers, see Figure 5.7. This gives us a relatively good value when the E-plane and H-plane phase centers have similar values [14, pp. 8-76], which is the case with pyramidal horns. We can see that this total phase center follows the radiation center closely, even for frequencies beyond the single mode band. When the phase centers from CST are regarded, we can see that the H-plane phase center follows the same phase center calculated by Muehldorf extremely well for middle frequencies. This is due to the radiation pattern being very stable in the H-plane. Side lobes and other deviations are only formed in the E-plane due to the excitation of the waveguide. The HPBW also changes more in the E-plane than the H-plane thus the results from E-plane CST simulation oscillate more.

5.2.2 Rectangular horn antenna

The rectangular horn simulated in this section is similar to the square horn from Section 5.2.1. The main difference is that the Rectangular horn aperture does not have equal sides which will yield greater difference between the analytically calculated E- and H-plane phase centers [17].

Rectangular Horn					
Length (mm)		132			
Waveguide length (mm)		45			
Aperture height H (mm)		82.3			
Aperture width W (mm)		107.1			
		H-plane		**E-plane**	
waveguide (mm)		23.5		11.8	
Aperture apex (mm)		20.5		30.5	
E-plane mode index	m	1	0	2	1
H-plane mode index	n	0	1	0	1
Mode cut-off frequency (GHz)		6.38	12.70	12.75	14.21

Table 5.2: Specification of the simulated rectangular aperture horn antenna. The distances for the aperture apexes are given from the back of the waveguide feed.

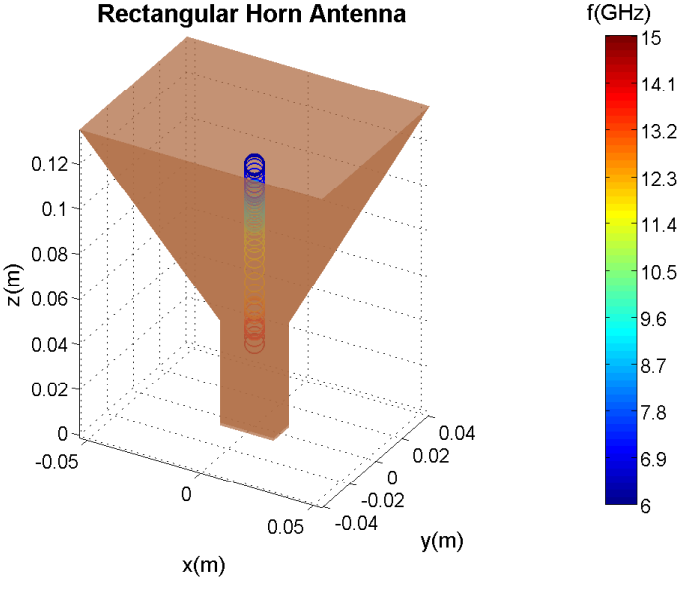

Figure 5.8: Radiation center of a rectangular aperture horn antenna.

Similar to the square aperture horn antenna, the radiation center follows the expected pattern, descending into the horn as the frequency is increased, in Figure 5.8. The radiation center is very stable in the horizontal directions, hence these directions will not be included in more detail.

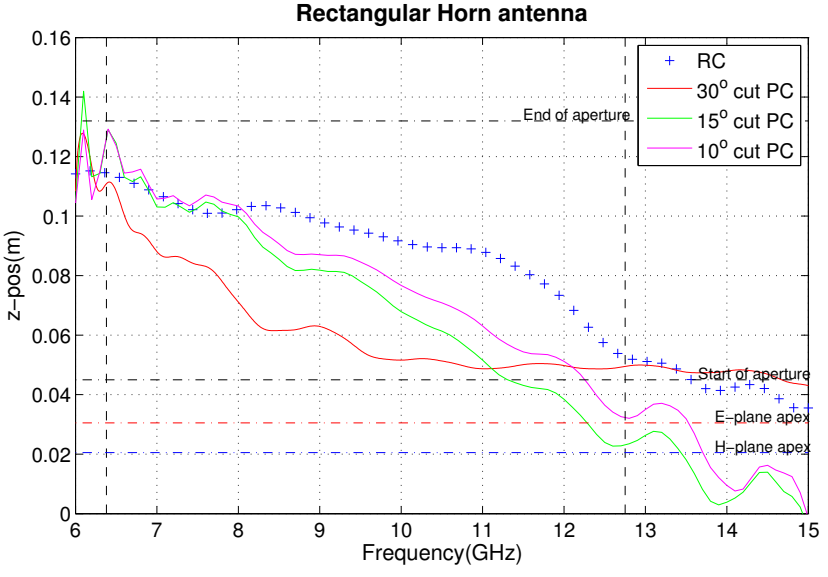

Figure 5.9: A comparison between the radiation center and the CST phase center along the length of the horn where the origin has been defined at the back of the horn antenna. The two vertical dashed black lines denote the first and second cut-off frequencies of the feeding waveguide. The HPBW varies from 35 degrees for low frequencies to 18 degrees for high frequencies.

In Figure 5.9 the CST results for the rectangular horn antenna oscillate far less than those calculated for the square horn antenna in Figure 5.6. They do, however, follow the same trend. The wide cut of 30 degrees drops down drastically to 50 mm in the beginning and is then rather constant over the rest of the simulation. Whereas the narrower cuts decrease relatively linearly. The radiation center has a higher position over most of the bandgap for this antenna and does not adhere closely to the CST results, except for low frequencies. There is a marked drop off in the radiation centers position at 12 GHz, which could be due to the rise of other modes in the waveguide.

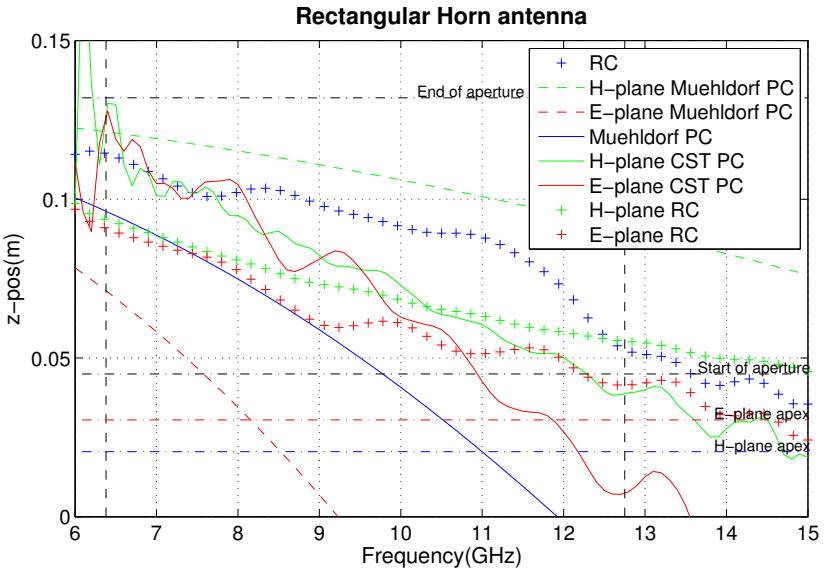

Figure 5.10: A comparison between the radiation center, the phase center calculated theoretically by the Muehldorf method an simulated data from CST. The two vertical dashed black lines denote the first and second cut-off frequencies of the feeding waveguide; note that the Muehldorf phase center is calculated solely with the first mode.

In Figure 5.10 we see that the Muehldorf phase center differs greatly between the two planes due to the different lengths of the aperture sides. The Muehldorf phase center deviates, even though the horn is almost pyramidal. Neither of the simulated values correspond well to Muehldorf for this antenna. The trait shared by the simulation methods is that the E- and H-plane centers have very similar values. This is quite opposite to the Muehldorf result and speaks to the similarities between the planes. This horn is in fact more pyramidal than the square horn, which can be seen in Table 5.2, as the imaginary aperture apexes for the different planes are closer together than for the square horn in Table 5.1. Note that both of the separate plane radiation centers have lower values than that of the total radiation center. Thus the method of taking the average of the two planes to find the total phase center does not apply to the radiation center.

5.2.3 Sectoral Horns

Sectoral horns are horn antennas with apertures that flare only in one direction. They are interesting as they are a common example when illustrating classical phase center calculation methods, such as the one presented by Muehldorf, see Section 4.6.3. The phase center in the plane which the aperture does not flare is constant and can be found approximately at the aperture's edge [10].

Sectoral H-plane Horn					
Length (mm)		148			
Waveguide length (mm)		48			
Aperture height H (mm)		25			
Aperture width W (mm)		150			
		H-plane		**E-plane**	
Waveguide (mm)		50		25	
Aperture apex (mm)		-2		∞	
E-plane mode index	m	1	2	0	1
H-plane mode index	n	0	0	1	1
Mode cut-off frequency (GHz)		3.00	6.00	6.00	6.70

Table 5.3: Specification of the simulated Sectoral H-plane aperture horn antenna. The distances for the aperture apexes are given from the back of the waveguide feed.

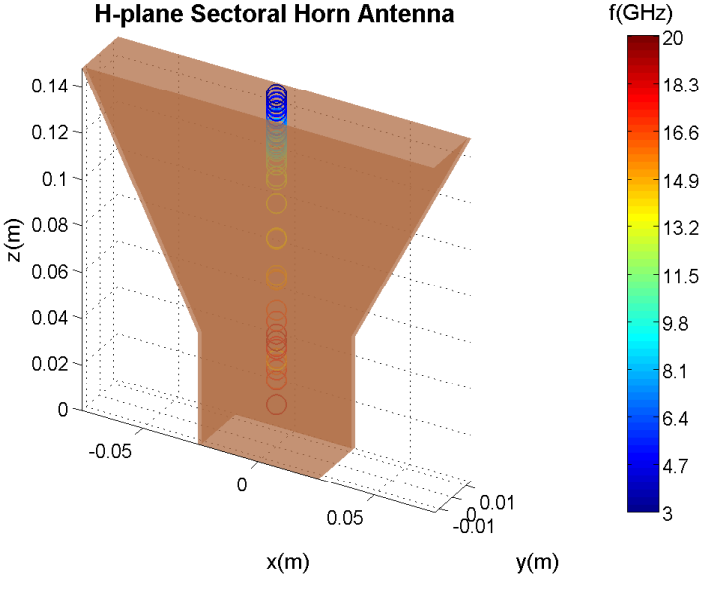

Figure 5.11: Radiation center of an H-plane sectoral horn antenna.

In Figure 5.11 the radiation centers position is close to the edge of the horn for the single-mode frequencies between 3–6 GHz. The radiation center only drops down into the horn as the frequency is increased well beyond the second mode cut-off frequency. This may indicate that the E-plane phase has a greater influence on the radiation center position than the H-plane. The classical methods predict that the E-plane phase center should be constant at the horn aperture [10], here the radiation center follows that behaviour over most of the bandgap.

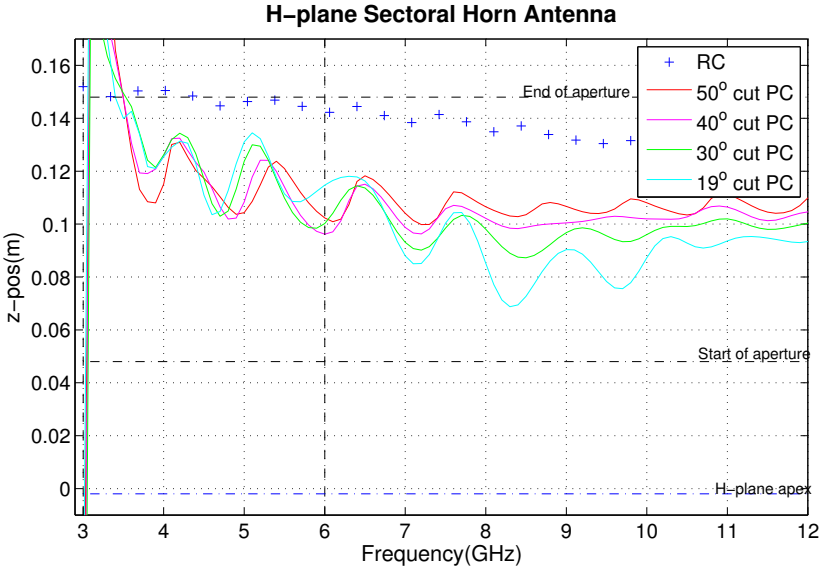

Figure 5.12: A comparison between the radiation center and the phase center calculated in CST with various cut angles; where the origin has been defined at the back of the simulated structure. The two vertical dashed black lines denote the first and second cut-off frequencies of the feeding waveguide. The HPBW varies between 100 and 35 degrees in the E-plane for this antenna, and between 40-20 degrees in the H-plane.

The phase center and radiation center in Figure 5.12 do not coincide. The radiation center behaves according to the predicted behaviour of the E-plane phase center, staying relatively constant at the edge of the aperture. The phase center on the other hand oscillates heavily and lies somewhere in the middle of the horn. This is an effect of having a big difference between the E- and H-plane phase centers. The method of calculating a total phase center by averaging between the three planes then produces strange results.

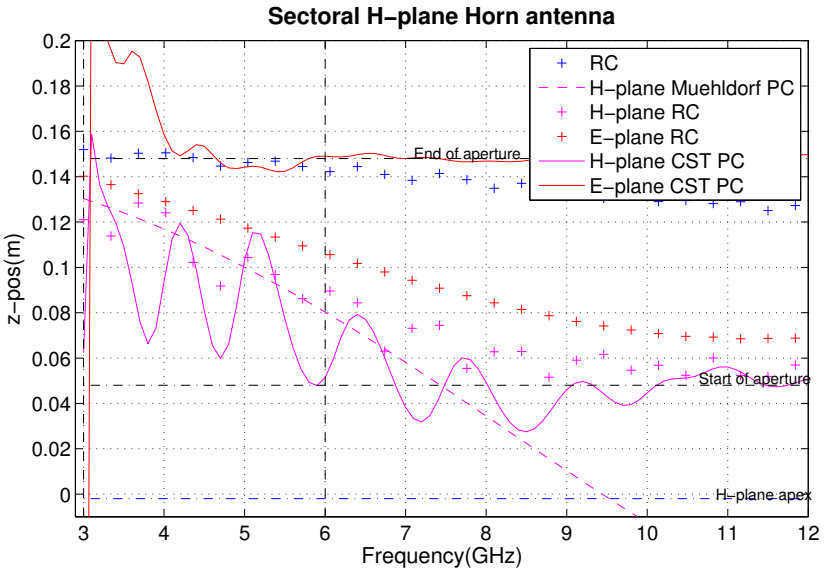

Figure 5.13: A comparison between the radiation center, the Muehldorf phase center and the CST phase center. The Muehldorf E-plane phase center is not calculated as the imaginary aperture apex is infinitely far away in the E-plane. The Muehldorf E-plane phase center coincides with the end of the aperture shown in the figure at 148 mm. The two vertical dashed black lines denote the first and second cut-off frequencies of the feeding waveguide.

In Figure 5.13 we see that the radiation center and the E-plane CST phase center coincide very well. This further strengthens the observation that the radiation center is dominated by E-plane effects. For a sectoral H-plane horn the main lobe is much wider in the E-plane than the H-plane, due to the excitation of the waveguide. As a consequence, the radiation center emphasizes the phase variations in the E-plane more than the phase center does. We can also see that the oscillations in the phase center in figure 5.12 come mainly from the H-plane phase center. If we observe the H-plane radiation center we see the same oscillations there, albeit with lower amplitude. These oscillations originate from an uneven phase in the H-plane, an example of the phase function for this antenna can be found in Figure 5.32. Between the first and second mode cut-off frequencies the H-plane radiation center coincides well with the value calculated by Muehldorf.

Sectoral E-plane Horn					
Length (mm)		148			
Waveguide length (mm)		48			
Aperture height H (mm)		150			
Aperture width W (mm)		50			
		H-plane		**E-plane**	
Waveguide (mm)		50		25	
Aperture apex (mm)		∞		28	
E-plane mode index	m	1	2	0	1
H-plane mode index	n	0	0	1	1
Mode cut-off frequency (GHz)		3.00	6.00	6.00	6.70

Table 5.4: Specification of the simulated Sectoral E-plane aperture horn antenna. The distances for the aperture apexes are given from the back of the waveguide feed.

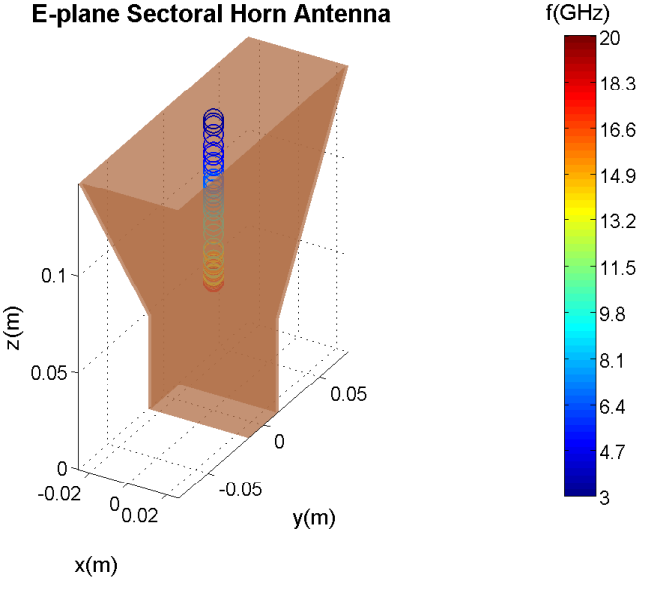

Figure 5.14: Radiation center for a E-plane sectoral horn antenna.

In contrast to the H-plane sectoral horn the radiation center's position descends evenly into the horn for low frequencies in Figure 5.14. The radiation center only starts to deviate from this behaviour at very high frequencies, far above the second mode cut-off frequency. This behaviour is due to the fact that this horn flares in the E-plane and as such the E-plane radiation gives rise to a moving phase center. The radiation center, as discussed above, is mainly influenced by the radiation with high amplitude. The excitation of the waveguide leads to a much wider radiation pattern in the E-plane than H-plane, thus the E-plane radiation influences the radiation center more.

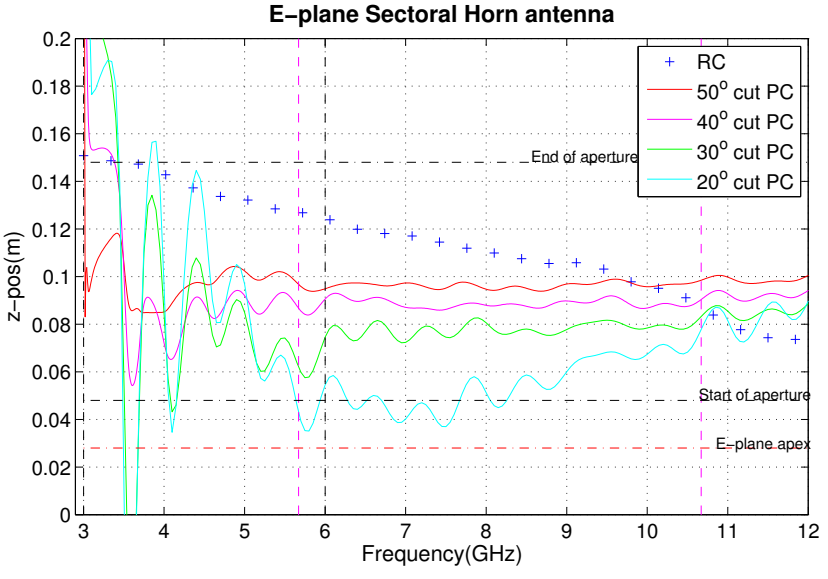

Figure 5.15: The figure shows a comparison between the radiation center and the phase center calculated in CST with various angular cuts. The two vertical dashed black lines denote the first and second cut-off frequencies of the feeding waveguide. The main radiation lobe splits in two for this antenna at the frequencies between the two vertical purple lines at 5.67-10.67 GHz due to the rise of higher order modes in the waveguide. Such a split compromises the classical phase center calculations as they run the risk of minimizing parts of the phase which correspond to low amplitude radiation. The theoretical H-plane radiation center is at the end of the aperture. The HPBW varies between 50 and 20 degrees in the E-plane for this antenna, and between 60-25 degrees in the H-plane.

In Figure 5.15 we see that the radiation center does not coincide well with the phase center. The phase centers oscillate heavily except for the wide cuts and only stabilize after the second mode cut-off frequency. These stabilized values are however in the region where the main beam splits in two, thus they cannot be trusted as the CST phase center calculation relies on having a well defined main beam. In contrast, the radiation center describes a very stable curve descending into the horn relatively linearly. The wide cuts seem to be stable at the middle of the horn, this behaviour is not predicted by previous theories [10].

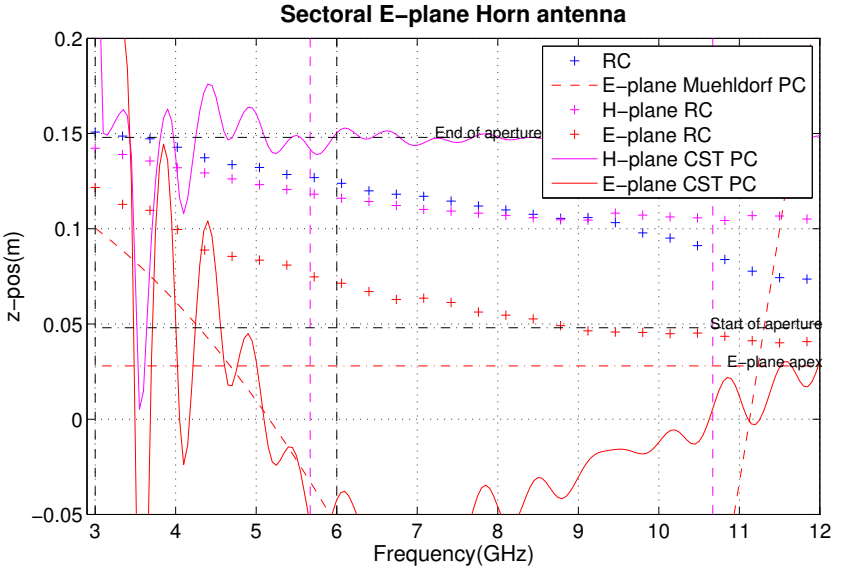

Figure 5.16: A comparison between the Muehldorf phase center, the CST phase center and the radiation center. The two vertical dashed black lines denote the first and second cut-off frequencies of the feeding waveguide. The main radiation lobe splits in two for this antenna at the frequencies between the two vertical purple lines. Such a split compromises the classical phase center calculations as they no longer have well defined phase function to minimize. The horizontal black line denotes the edge of the aperture. The Muehldorf H-plane phase center is situated at the edge of the aperture.

We see in Figure 5.16 that both the E- and H-plane CST phase centers oscillate heavily before the second mode cut-off frequency. The radiation center is not close to either the CST or the Muehldorf phase center. We can see that the H-plane CST phase center is relatively constant at the aperture after the second mode cut-off frequency, whereas the E-plane phase center drops off quickly. The E-plane CST phase center drops off far below the imaginary E-plane apex which is not supported by previous theories [17][14, ch. 8]. At high frequencies the E-plane CST phase center seems to rise again but is still situated below the imaginary aperture apex. The CST phase center calculation for this antenna is very uncertain, as it oscillates heavily and the main beam splits in two. The radiation center, on the other hand, gives us very stable results, which support the validity of the result.

5.2.4 Circular horn antenna

The circular aperture horn antenna is used by CST as an introductory example to antenna simulations. The phase and radiation center calculations have been included here as a reference.

Circular Horn					
Length (mm)		69.9			
Waveguide length (mm)		12.7			
Aperture radius (mm)		25.4			
		H-plane		**E-plane**	
Waveguide (mm)		25.4		12.7	
E-plane mode index	m	1	0	2	1
H-plane mode index	n	0	1	0	1
Mode cut-off frequency (GHz)		5.90	11.80	11.80	13.20

Table 5.5: Specification of the simulated circular aperture horn antenna.

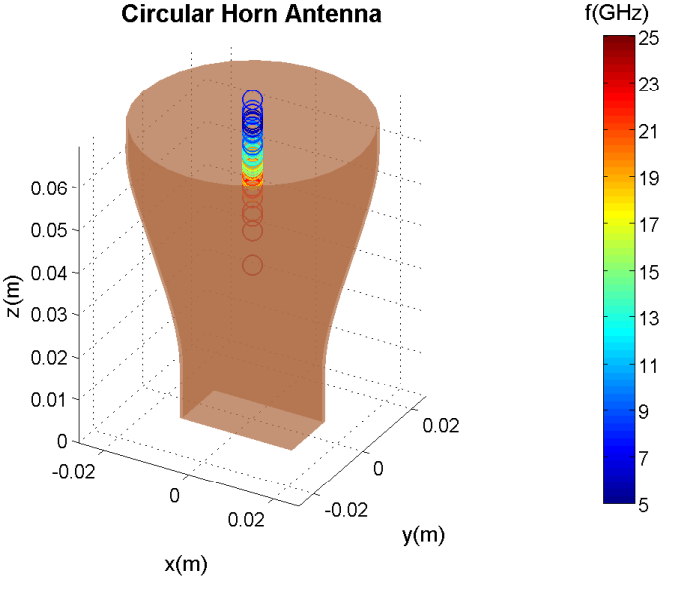

Figure 5.17: Radiation center for a circular horn antenna.

The radiation center positions seem to be clustered at the aperture for single mode frequencies in Figure 5.17. Only for frequencies far above the second mode cut-off frequency, found in Table 5.5, does the radiation center descend into the horn. We can also see that there are some oscillations present for mid-frequencies.

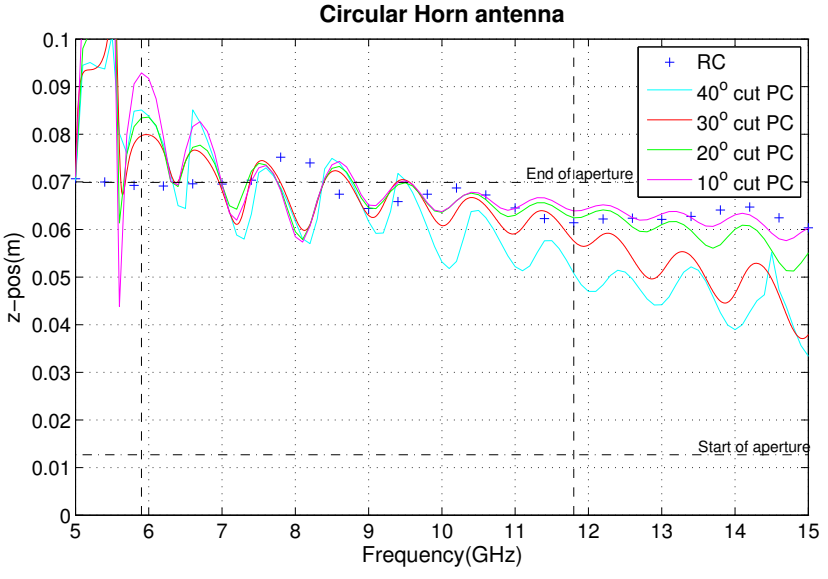

Figure 5.18: A comparison of the radiation and phase center position along the length of the circular horn antenna. The two vertical dashed black lines denote the first and second cut-off frequencies of the feeding waveguide. The HPBW varies between 60 and 16 degrees.

In Figure 5.18 we notice that radiation center lies very close to the edge of the aperture between the first and second mode cut-off frequency. In the interval $[7, 8]$ GHz the radiation center rises outside of the horn, which is not predicted by theory. Heavy oscillations are present in the phase centers position for most frequencies. The radiation center oscillates also, but not as regularly as the phase center and with far less amplitude. Despite these oscillations the phase and radiation center fall in the same region between the first and second cut-off frequencies.

5.3 Printed planar structures

Planar antenna structures are most commonly used for their low profile and volume. They are also cheap to manufacture and easy to integrate in planar circuits. These qualities generally come with a trade-off in Impedance and radiation efficiency [12, ch. 37].

5.3.1 Patch antenna

A patch antenna consists of a metal plate on a slab of dielectric material separating the plate from the ground plane. The plate is fed through a probe or similar feeding structure. The patch antenna is a very common type of antenna normally implemented in array designs.

Patch antenna	Square	Rectangular
Width (mm)	50	75
Length (mm)	50	50
Patch resonance (GHz)	1.9	1.9

Table 5.6: Specification of the simulated Patch antennas

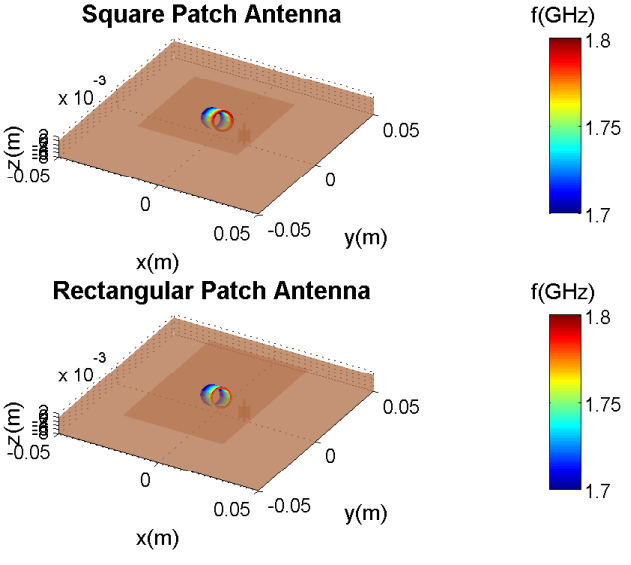

Figure 5.19: The radiation center as a function of frequency for the simulated patch antennas.

In Figure 5.19 we see that the radiation center varies only along the main current direction of the patch, the x-direction. The width of the metal plate is often increased to increase the bandwidth of the patch antenna. Such a change ha little effect on the behaviour of the radiation center as can be seen in the lower part of Figure 5.19.

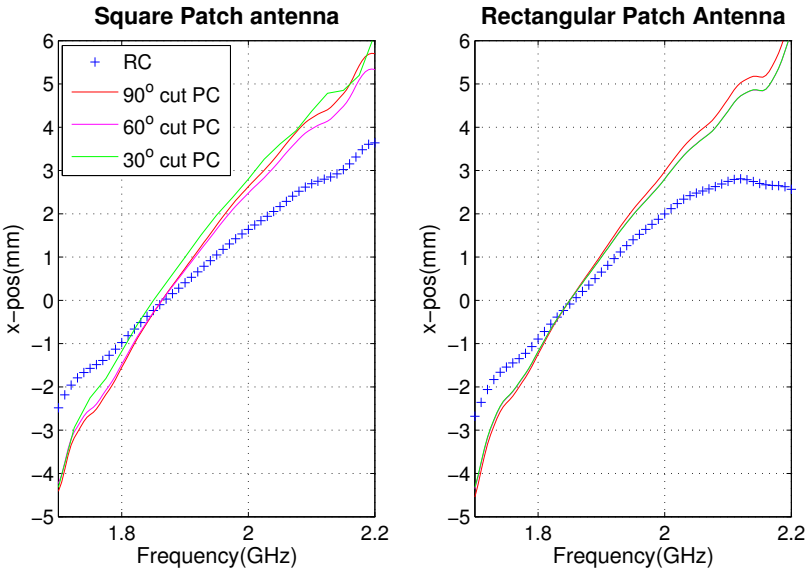

Figure 5.20: The radiation centers position along the length of the patch antennas. The HPBW of these antennas varies between 120 and 85 degrees.

For the square patch antenna in Figure 5.20, we observe that the shape of the radiation center curve is roughly the same as the phase center curve. However, the amplitude of the radiation center curve is smaller and varies only between -2 and 4 mm, instead of -4 and 6 mm as the phase center. For the rectangular patch antenna, the radiation center and the phase center differ more compared to the similar curves for the square patch. The radiation center also varies less for the rectangular patch than for the square patch antenna, the increased width of the patch antenna seems to compress the radiation centers position. The phase center of the rectangular patch on the other hand is almost identical to the phase center of the square patch antenna.

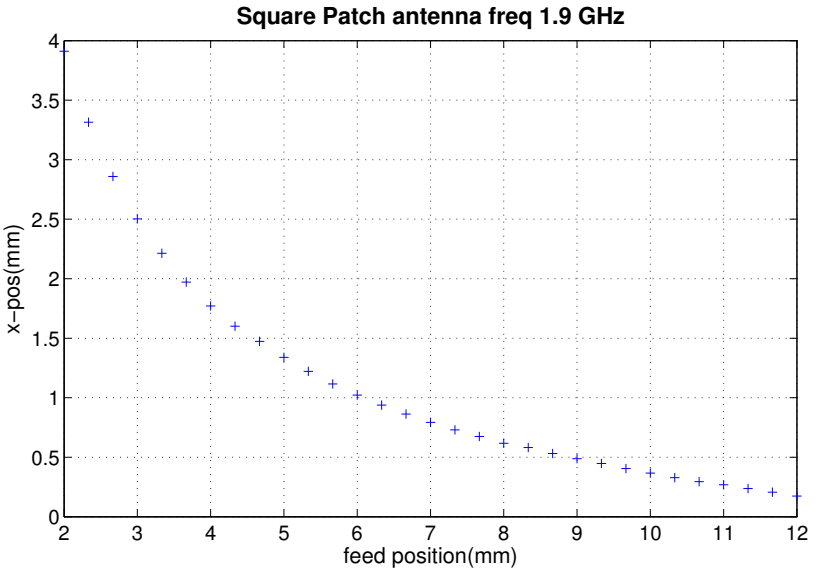

Figure 5.21: Shows how the radiation center varies when the feed position is shifted. The feed position was shifted along the patches resonant axis, the value is measured from the middle of the patch.

The patch antenna feed is often varied along the antenna to find the correct input impedance, Figure 5.21 shows how the radiation center is affected by such a variation. In the figure we can see that the radiation center position attenuates exponentially as the feed position is moved towards the edge of the patch.

5.3.2 Spiral antenna

Spiral antennas are small structures that operate over very large bandwidths. For different frequencies different parts of the antenna structure are active. At high frequencies currents are induced close to the center of the antenna, for low frequencies areas further away form the center are activated. Spiral antennas have significant pulse distortion which is believed to be characterized by a moving phase center [22]. Hence it is interesting to see if the radiation center coincides with this belief.

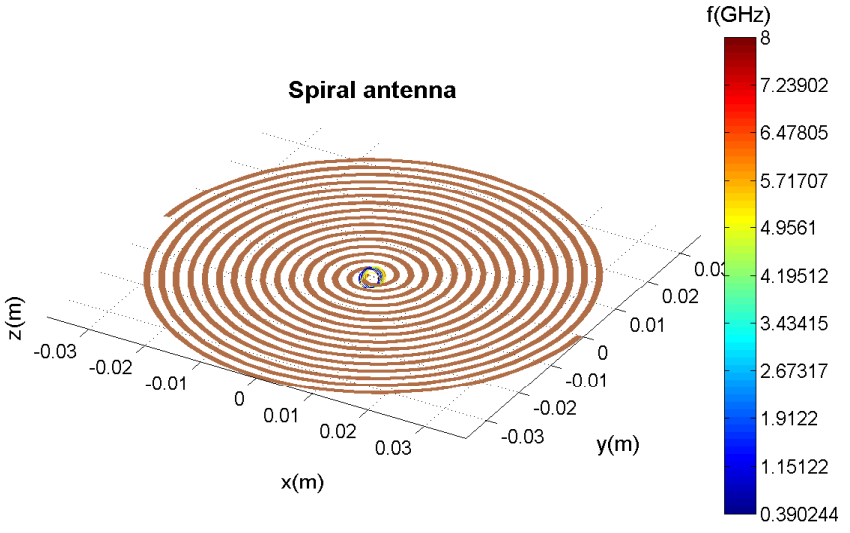

Figure 5.22: Radiation center of the simulated Spiral antenna.

In Figure 5.22 we can see that the radiation center of the simulated spiral antenna is fixed in its center for all frequencies. This does not fit at all with the predictions for the phase center. This could be due to the fact that the antenna radiates symmetrically up and down, thus the movement inducing effects of the radiation cancel out.

5.4 Endfire dipole arrays

5.4.1 Log-periodic dipole array antenna

The log-periodic antenna is a structure made from dipoles with lengths that vary logarithmically. In contrast to other similar structures, such as the Yagi-Uda antenna with one active element, these dipoles are galvanically connected. This gives the antenna a wide bandwidth as the dipoles are resonant for different frequencies. As a certain dipole starts to resonate the phase center should move closer to it, making the phase center vary across the structure over frequency. The expected behaviour of the antenna is thus that the phase center should fall in the region of the resonant dipole.

Log-periodic antenna	
Resonance of first dipole (GHz)	1.93
Resonance of last dipole (GHz)	4.68
Length (mm)	189.24

Table 5.7: Specification of the simulated Log-periodic antenna.

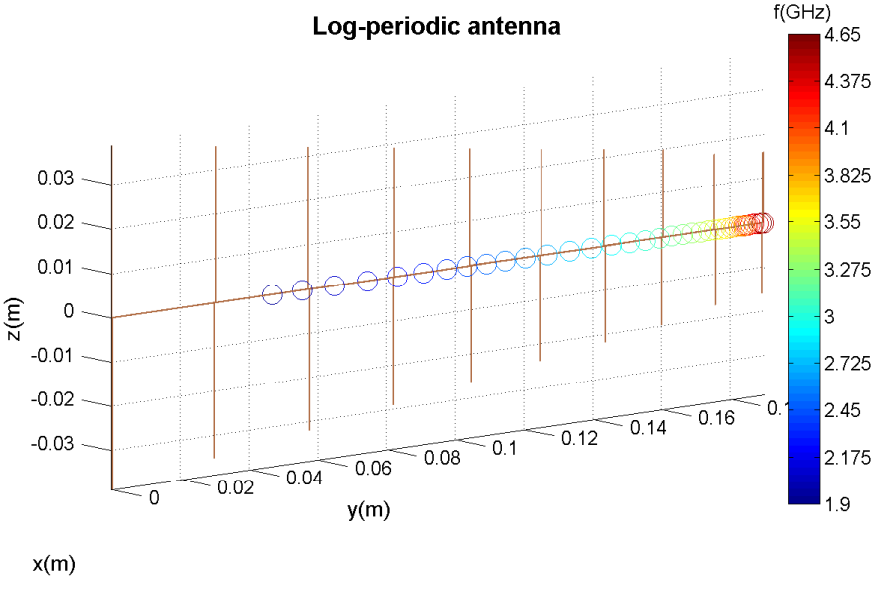

Figure 5.23: The radiation center of the log-periodic antenna.

The first dipole in this log-periodic antenna is resonant at 1.9 GHz, as seen in Table 5.7. For low frequencies Figure 5.23 shows that the radiation center does not correspond to the resonant dipoles position but is shifted towards the other dipole elements of the antenna. This continues linearly up to high frequencies where the radiation center's position shifts less and less. This behaviour is due to the resonance in the other elements made stronger by their galvanic connection to the currently resonant dipole. The smaller antenna elements seem to pull harder on the radiation center than the larger elements do, evident by the fact that the radiation center is shifted a greater distance from its resonant element at low frequencies.

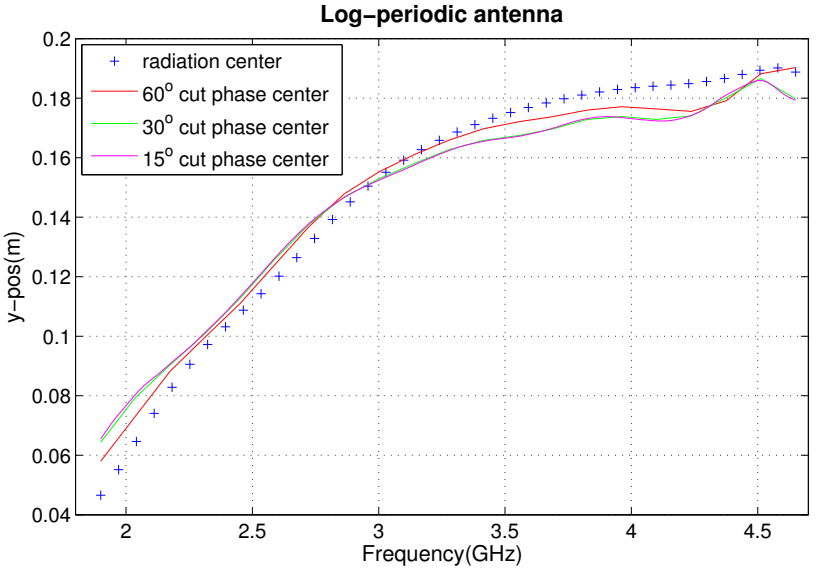

Figure 5.24: A comparison between the radiation center and the phase center as calculated by CST. The HPBW of this antenna varies between 160-90 degrees in the H-plane, and between 79-62 in the E-plane.

The phase and radiation centers agree extremely well in Figure 5.24. The various phase cuts in CST do not make a big difference in the calculation of the phase center. This is due to the log periodic antenna having a wide and well defined main beam which does not change much in shape and size over the antennas operational frequencies. Thus the CST calculation produce good results, as they do not include parts of the phase function which correspond to low amplitude radiation.

5.4.2 Yagi-Uda antenna

The Yagi-Uda antenna is a narrow band antenna with high directivity. These good qualities and its rather simple design mean that Yagi-Uda antennas are widely used. They consist of a single active element surrounded by parasitic elements known as directors and reflectors. There are usually only a few reflectors which are positioned behind the driven element, these are slightly longer than the active element. To the front there are several directors which are slightly shorter than the active element. Because of the resonance with these parasitic elements the phase center should not coincide with the active element.

Yagi-Uda antenna	
Directors	4
Reflectors	1
Director length (mm)	4
Reflector length (mm)	5.2
Driven element length (mm)	5
Length (mm)	5.7
Resonance (GHz)	35.1

Table 5.8: Specification of the simulated Yagi-Uda antenna.

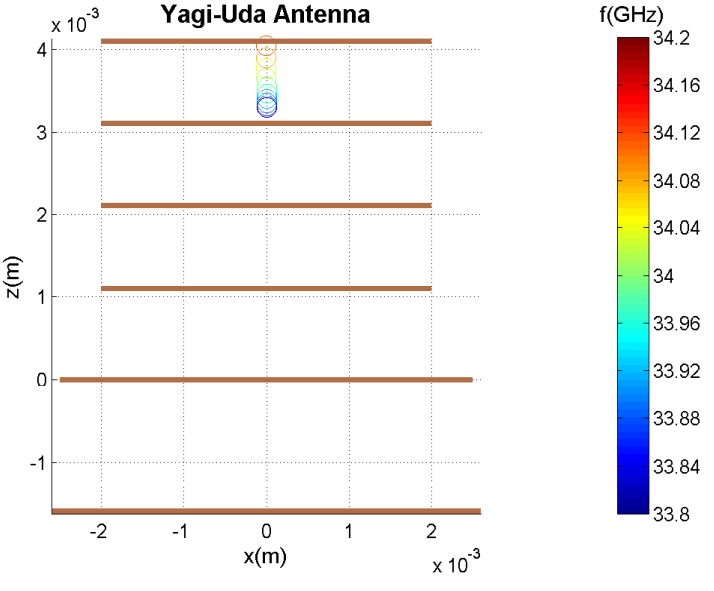

Figure 5.25: Radiation center of the simulated Yagi-Uda antenna.

The radiation center in Figure 5.25 lies within the bounds of the antenna. We see that the position is shifted away from the active element as expected.

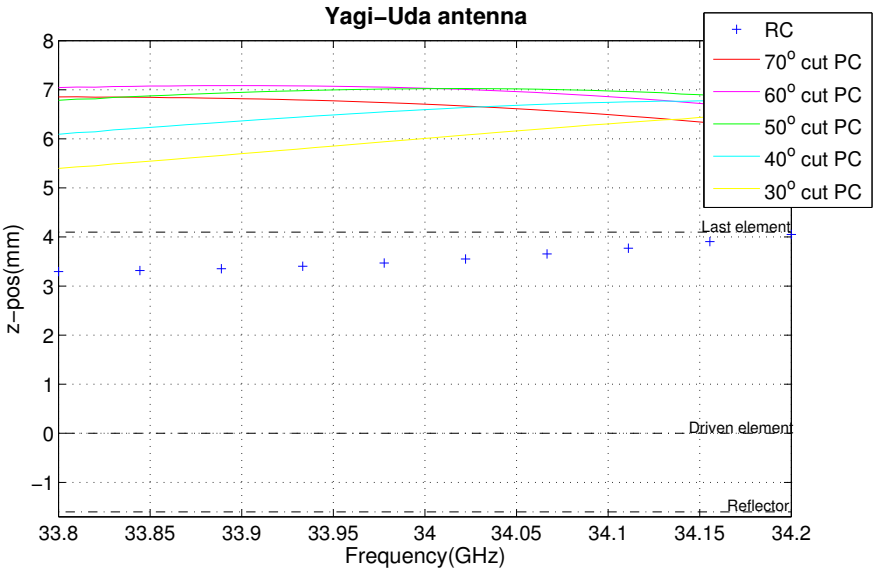

Figure 5.26: A comparison between the phase and radiation center for the Yagi-Uda antenna. The HPBW of this antenna is about 50 degrees.

Figure 5.26 depicts the differences in the location of the phase and radiation centers for the Yagi-Uda antenna. The phase center is located far outside the antenna structure which is not impossible, but not predicted. The radiation center on the other hand lies in a much more realistic region of the antenna.

5.5 Leaky Lens antenna

The specifications of this Lens antenna can be found in [18, 19]. Here the lens antenna is included in this thesis as an example of an advanced antenna structure where the phase center position is of interest, but the classical methods fail to provide feasible answers. The phase center of a lens antenna should fall inside of the structure, as this is where it has its focus. In Figure 5.27 we see that the radiation center meets this expectation. Figure 5.28 shows how the phase and radiation center vary with frequency for the leaky lens antenna along its directional axis. It is clear that the phase center falls well outside the lens antenna, to positions which are not realistic. This supports the validity of the radiation center calculation as it can produce probable results for this type of antenna.

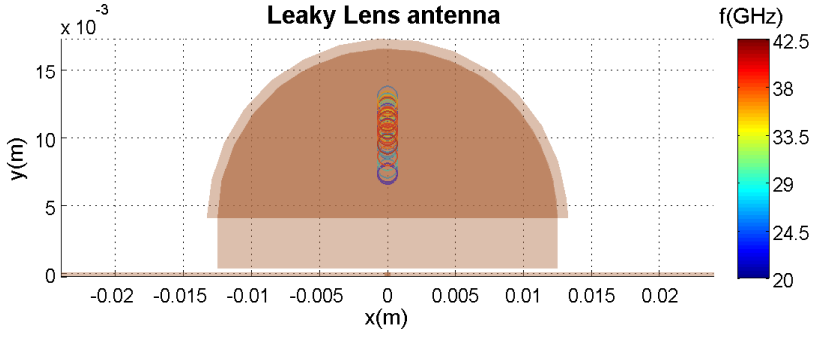

Figure 5.27: The radiation center of the simulated leaky lens antenna.

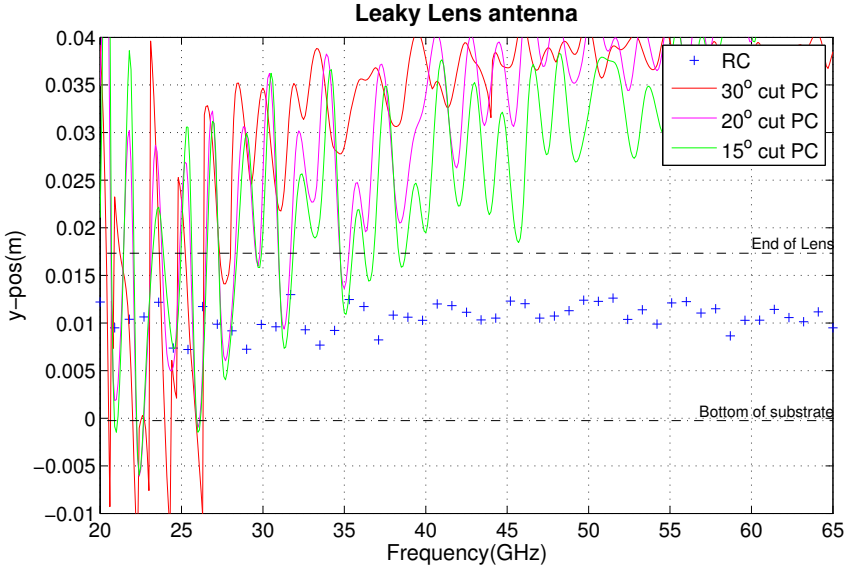

Figure 5.28: A comparison between the phase and radiation center along the main direction of the lens antenna.

5.6 Phase comparison

In the previous sections we evaluated the position of the radiation center and the phase center for a set of different antennas. In this section we will look at the actual phase function in the main beam when the far-field has been translated to the phase or radiation center. This is interesting as the goal of the phase and radiation center is to minimize the phase. For brevity only some of the antennas will feature in this section. We will only investigate the phase at a single frequency for the chosen antennas. This is done in order to get a general sense of how great the differences between the centers are.

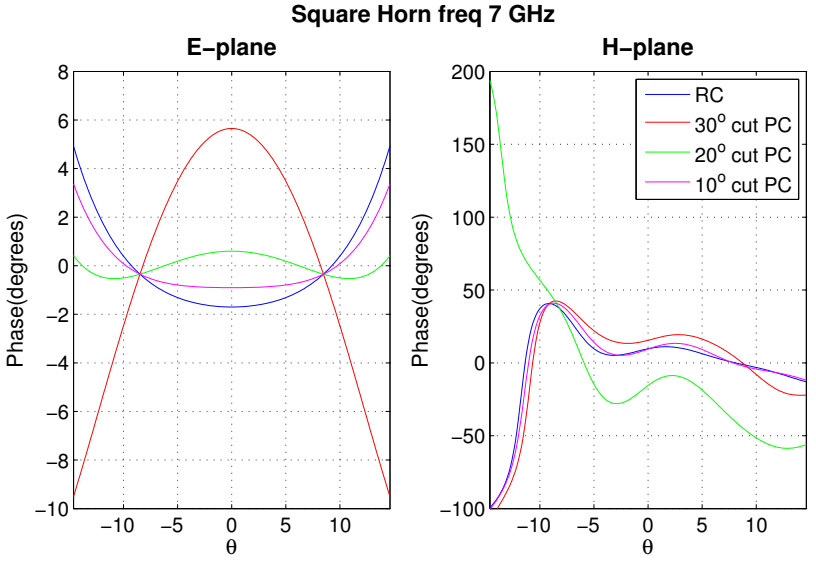

Figure 5.29: A comparison of the phase function inside the HPBW of the far-field when translated to the radiation and phase centers for the square aperture horn antenna.

The phase variation in the E- and H-plane is very different in Figure 5.29, the H-plane phase varies several magnitudes more than the E-plane phase. In the E-plane phase we can clearly see that the 30° cut has the least smooth phase. The thinner phase center cuts have less variation than the radiation center in the E-plane but not necessarily in the H-plane. The 20° cut has the greatest variation in the H-plane where the radiation center seems the smoothest.

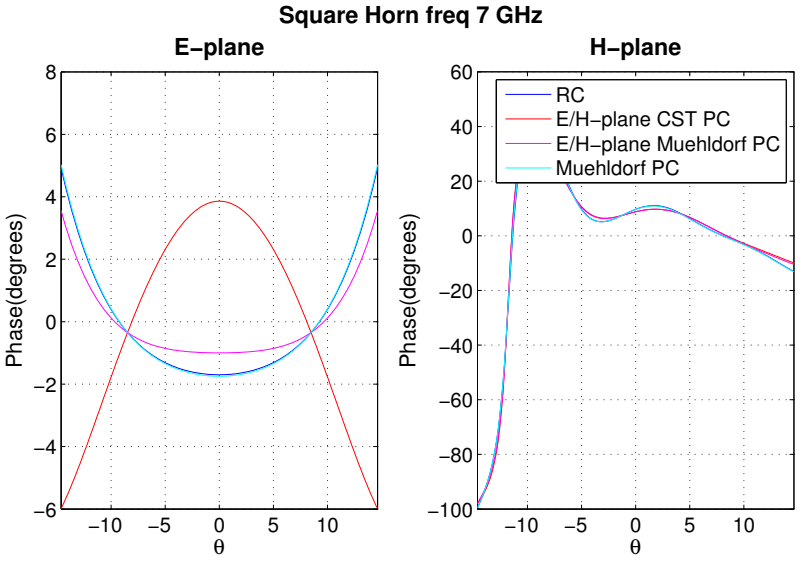

Figure 5.30: A comparison of the phase function inside the HPBW for the Square horn antenna when it has been minimized by the radiation center,CST phase center and Muehldorf phase center.

The H-plane phase function in Figure 5.30 is very similar for the different centers. In the E-plane the magnitude of variation is much less than the H-plane, but the differences between the centers are much more pronounced. The CST phase function is the most uneven in the E-plane, where as the Muehldorf E-plane phase center achieves the smoothest phase. However, the actual differences are very small, meaning that all centers seem to minimize the phase well.

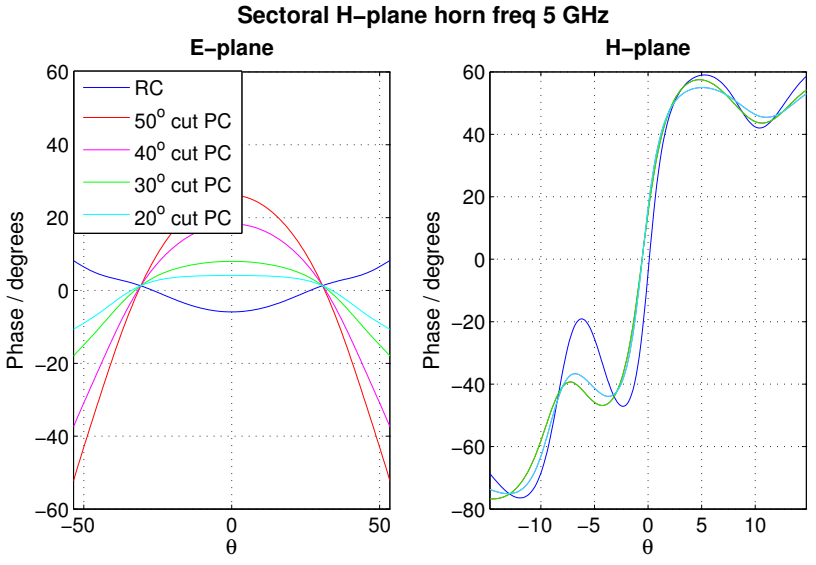

Figure 5.31: A comparison of the phase function inside the HPBW of the far-field when translated to the radiation and phase centers of the sectoral H-plane aperture horn antenna. Note that the angular width of the HPBW is different in the two planes.

In Section 5.2.3 we showed that the radiation center calculation was influenced by the radiation in the E-plane than the H-plane. For the Sectoral H-plane horn, Figure 5.31 shows that the magnitude of the phase variation is similar in the E- and H-plane. All centers seem to minimize the phase equally in the H-plane. In the E-plane the radiation center and the narrower CST cuts seem to minimize the phase well, whereas the wider cuts give more even phase functions.

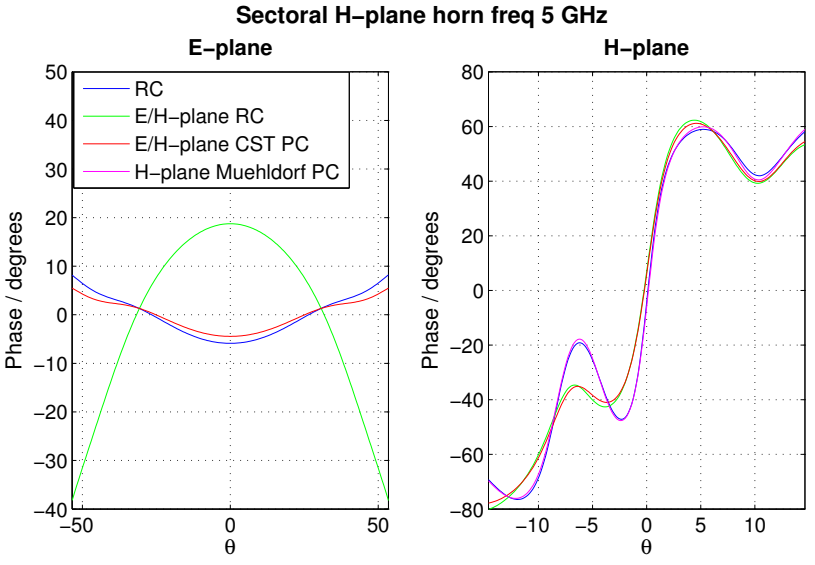

Figure 5.32: A comparison of the phase function inside the HPBW of the Sectoral H-plane horn when minimized by the radiation center, CST phase center and the Muehldorf phase center. Note that the angular width of the HPBW is different in the two planes.

In Figure 5.32 we can see that the E-plane truncated radiation center does not minimize the phase particularly well. The CST E-plane phase center and the total radiation center seems to minimize the phase most effectively in the E-plane. None of the centers seem better or worse at minimizing the phase in the H-plane. Figure 5.32 suggests that the truncated radiation center does not achieve its purpose, to minimize a specific phase, particularly well.

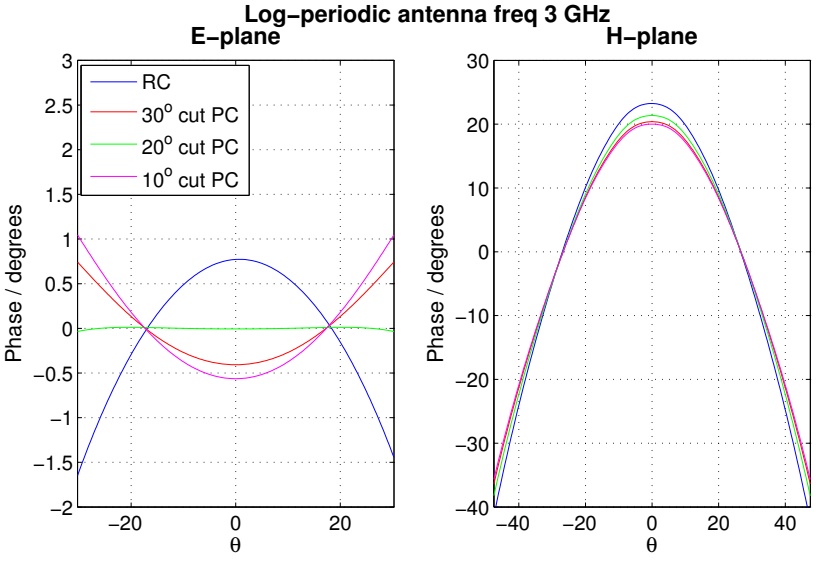

Figure 5.33: A comparison of the phase function inside the HPBW of the far-field when translated to the radiation and phase centers of the Log-periodic antenna. Note that the angular width of the HPBW is different in the two planes.

The phase variation of in the E-plane of Figure 5.33 is extremely small. The phase minimized by the radiation center seems to vary the most but still only a couple of degrees. In the H-plane the phase variation is significantly larger but there is hardly any difference between the centers.

Chapter 6
Discussion

Throughout the simulations that have been carried out in this thesis it has been obvious that the angular momentum method does not consistently produce the same results as classical phase center calculations. However, it is possible that this is purely because the radiation center minimizes the phase better than the phase center. For antennas where the phase center is well defined, e.g. the Log-periodic antenna see Section 5.4.1, the radiation and phase center coincide very well. For other antennas, such as the Sectoral horn antennas in Section 5.2.3, the CST phase center calculations produce very unstable curves where the radiation center varies smoothly. For some antenna structures, the phase center calculations produce results far outside of the possible bonds, e.g. the Leaky Lens antenna see Section 5.5.

One of the most important antennas when discussing the phase center is the horn antenna, because it is often characterized by its phase center. In Section 5.2.1 we notice the radiation center coincides fairly well with CST phase center results, as well as Muehldorf calculations for a square aperture horn antenna. However, the rectangular horn antenna is only slightly different from the square horn antenna and yet we see much greater differences in Section 5.2.2. These differences become more prominent as the ratio between the aperture height and width is changed further with the sectoral horn antennas in Section 5.2.3. When the difference between the height and the width is increased the width of the radiation lobe increases in the E-plane and decreases in the H-plane. CST only allows for one cut angle to be selected when calculating the phase center, this results in the calculation ignoring some of the high amplitude radiation in the E-plane. The radiation center calculation on the other hand does not have this problem, since it evaluates the entire phase function with the angular momentum. Thus the radiation center's behavior follows the phase center of the plane with the widest radiation lobe. Evidence of CSTs single cut angle influencing results can be seen elsewhere as well. Specifically, the horn antenna results differ in stability. Where the phase center seems to oscillate, particularly when the phase cut is incorrectly chosen, the radiation center produces relatively smooth curves for all types of horns. The radiation center does not seem to excel in the truncated calculations. The E- and H-plane truncated radiation center does not match the predicted behaviour of the E- and H-plane phase centers for the sectoral horn antennas in Figures 5.13 and 5.16. The truncated radiation center does not seem to minimize the phase function effectively in Figure 5.32. The general radiation

center minimizes the phase more effectively even though the truncated radiation center is only calculated by the radiation in the plane.

For some of the other antennas the results were not as obvious, e.g. the spiral antenna. Previous theories predict that the phase center of the spiral antenna should move with frequency as the spiral antenna has significant pulse distortion [22]. The radiation center does not match this prediction at all and is fixed in the center of the antenna for all frequencies. This could be due to the fact that the spiral antenna radiates symmetrically from its top and bottom, canceling out any movement of the radiation center. In normal implementation spiral antennas usually feature an absorber on one of their sides in order to only radiate in one direction. Such an absorber could lead to a variation in the radiation center position. However, simulating such a structure falls outside the scope of this thesis.

The results from the patch antenna simulations in Section 5.3.1 are not clear cut either. The phase center does not seem to vary with the width of the patch whereas the radiation center does. This could be due to the difference in how the phase information is extracted. In the CST phase center calculations, see Section 4.6.2, the phase function is minimized directly. The radiation center calculations on the other hand minimizes the phase indirectly through the far-field amplitude in Equation (4.4.3). The far-field amplitude is derived directly from the currents on the antenna structure in Equations (4.1.20) and (4.1.16). When the width of the patch is changed, the current distribution changes, which could lead to the difference in radiation center position. Investigating the radiation center's relation to the surface current falls to future work.

In Section 5.6, we regarded the actual phase function after minimization by the radiation center and the phase center. These examples are interesting as they indicate that the radiation center minimizes the phase well in the main lobe. However, in most of the examples the phase center has slightly less variation in the phase than the radiation center. While such a small range of examples is not enough to draw any final conclusions, they seem to indicate that the radiation center fulfills its intended role.

Chapter 7
Conclusions

The goal of this thesis was to investigate if the radiation center is a suitable replacement for the phase center in terms of origin of the radiated field. For antennas where the phase center is well known, such as the horn antenna, we have seen the radiation center calculations produce plausible results. We have also seen the radiation center calculations achieve acceptable results for antennas where the phase center methods could not, e.g. the Leaky lens and Yagi-Uda antenna. Additionally the radiation center posseses qualities which the phase center lacks.

The radiation center can be implemented on any antenna structure.
For phase center calculations the antenna needs to have a well defined main beam, the radiation center calculation on the other and uses the entire sphere of radiation to calculate its position.

The radiation center does not need user input in its calculation.
A big disadvantage in current phase center calculations is the need for user input. The results of the calculation vary wildly with user input, as can be seen in the results presented in Chapter 5.

Finally, when the explicit phase cuts were examined in Section 5.6 we saw that the radiation center minimized the phase function in the main lobe almost as well as the phase center. We can thus conclude that the radiation center is a prime candidate for origin of radiation for antennas.

Chapter 8

Future work

The work done in this thesis has indicated additional areas of research in investigating the radiation center.

Investigating a method for evaluating the smoothness of the phase function.

How do we tell if the radiation or phase center has minimized the phase best? A method of evaluating how well the phase is minimized would greatly help in determining if the radiation center should replace the phase center.

Further investigation into the effect of angular truncation on the radiation center.

Does the radiation center minimize the phase in a plane well if its data is truncated to that plane?

Investigation into the current dependence of the radiation center.

The theory of the radiation center is closely linked to the surface currents of the antenna. Investigating this relation could greatly help our understanding of the radiation center.

Simulating larger array antennas and calculating the radiation center of their elements.

In this thesis we were unable to calculate the radiation center of each element in an array antenna. This would be very interesting to investigate, as we would be able to see how the resonance between antenna elements in an array affected their electrical position. The electrical position is important as it can have a huge impact on sensitive measurements such as Direction of Arrival.

Investigate the physical implications of the $\cot\theta$ term in $\boldsymbol{a}_1$ (4.4.4).

It is unclear what this term represents or if it is unimportant physically. Understanding its presence will further our understanding of what the radiation center is.

Chapter 9
Appendix

Appendix A Vector Spherical Harmonics

The vector spherical harmonics are defined as,

$$\begin{cases} \boldsymbol{A}_{1lm}(\hat{\boldsymbol{r}}) = \dfrac{1}{\sqrt{l(l+1)}}\nabla \times (\boldsymbol{r}Y_{lm}(\hat{\boldsymbol{r}})) = \dfrac{1}{\sqrt{l(l+1)}}\nabla Y_{lm}(\hat{\boldsymbol{r}}) \times \boldsymbol{r}, \\ \boldsymbol{A}_{2lm}(\hat{\boldsymbol{r}}) = \dfrac{1}{\sqrt{l(l+1)}} r\nabla Y_{lm}(\hat{\boldsymbol{r}}), \end{cases} \tag{A.1}$$

where $\tau = 1, 2$, $l = 1, 2, ..., \infty$, and $m = -l, -l+1, ..., l$. The spherical harmonics $Y_{lm}(\hat{\boldsymbol{r}})(\theta, \phi)$ are defined as,

$$Y_{lm}(\theta, \phi) = \sqrt{\frac{2l+1}{4\pi}\frac{(l-m)!}{(l+m)!}} P_l^m(\cos\theta) e^{\mathrm{j}m\phi},$$

where $P_l^m(\cos\theta)$ are the Legendre polynomials [2]. The spherical vector harmonics and spherical harmonics are orthonormal on the unit sphere Ω,

$$\iint_\Omega \boldsymbol{A}_{\tau lm}(\hat{\boldsymbol{r}}) \cdot \boldsymbol{A}_{\tau' l' m'}(\hat{\boldsymbol{r}}) \mathrm{d}\Omega = \delta_{\tau\tau'}\delta_{mm'}\delta_{ll'},$$
$$\iint_\Omega Y_{lm}(\hat{\boldsymbol{r}}) Y_{l'm'}(\hat{\boldsymbol{r}}) \mathrm{d}\Omega = \delta_{ll'}\delta_{mm'}.$$

Appendix B Divergence and Laplace operators

The Laplace and divergence operators on the unit sphere are defined as,

$$\begin{cases} \nabla_\Omega = r\mathbf{P}_\Omega \cdot \nabla = \hat{\boldsymbol{\theta}}\dfrac{\partial}{\partial\theta} + \hat{\boldsymbol{\phi}}\dfrac{1}{\sin\theta}\dfrac{\partial}{\partial\phi}, \\ \nabla_\Omega^2 = \dfrac{1}{\sin\theta}\dfrac{\partial}{\partial\theta}\left(\sin\theta\dfrac{\partial}{\partial\theta}\right) + \dfrac{1}{\sin^2\theta}\dfrac{\partial^2}{\partial\phi^2}, \end{cases} \tag{B.1}$$

where $\mathbf{P}_\Omega = \mathbf{I} - \hat{\boldsymbol{r}}\hat{\boldsymbol{r}}$ is the projection operator on the unit sphere. Using these relations the $\mathcal{P}_\Omega\mathcal{L}^2$ operator acting on a transverse vector field $\boldsymbol{F}$ can be calculated using the definition of the Laplace operator [7],

$$\nabla^2\boldsymbol{F}(\hat{\boldsymbol{r}}) = \nabla(\nabla \cdot \boldsymbol{F}) - \nabla \times (\nabla \times \boldsymbol{F}). \tag{B.2}$$

By using the definitions of the divergence and rotation in spherical coordinates [2] equation B.2 can be expanded:

$$\begin{aligned}\nabla(\nabla\cdot\boldsymbol{F}) = \quad & \hat{\boldsymbol{r}}\left(-\frac{\partial F_\theta}{\partial\theta} - F_\theta\frac{\cos\theta}{\sin\theta} - \frac{1}{\sin\theta}\frac{\partial F_\phi}{\partial\phi}\right)\\ & +\hat{\boldsymbol{\theta}}\left(\frac{\partial^2 F_\theta}{\partial\theta^2} + \cot\theta\frac{\partial F_\theta}{\partial\theta} - (1-\cot^2\theta)F_\theta + \frac{1}{\sin\theta}\frac{\partial^2 F_\phi}{\partial\phi\partial\theta} - \frac{\cos\theta}{\sin^2\theta}\frac{\partial F_\phi}{\partial\phi}\right)\\ & +\hat{\boldsymbol{\phi}}\left(\frac{1}{\sin\theta}\frac{\partial^2 F_\theta}{\partial\phi\partial\theta} + \frac{\cos\theta}{\sin^2\theta}\frac{\partial F_\theta}{\partial\phi} + \frac{1}{\sin^2\theta}\frac{\partial^2 F_\phi}{\partial\phi^2}\right)\end{aligned} \tag{B.3}$$

$$\begin{aligned}\nabla\times(\nabla\times\boldsymbol{F}) = \quad & \hat{\boldsymbol{r}}\left(\frac{\partial F_\theta}{\partial\theta} + \cot\theta F_\theta + \frac{1}{\sin\theta}\frac{\partial F_\phi}{\partial\phi}\right)\\ & +\hat{\boldsymbol{\theta}}\left(\frac{1}{\sin\theta}\frac{\partial^2 F_\phi}{\partial\phi\partial\theta} + \frac{\cos\theta}{\sin^2\theta}\frac{\partial F_\phi}{\partial\phi} - \frac{1}{\sin^2\theta}\frac{\partial^2 F_\theta}{\partial\phi^2}\right)\\ & +\hat{\boldsymbol{\phi}}\left(-\frac{\partial^2 F_\phi}{\partial\theta^2} - \cot\theta\frac{\partial F_\phi}{\partial\theta} + (1+\cot^2\theta)F_\phi + \frac{1}{\sin\theta}\frac{\partial^2 F_\theta}{\partial\phi\partial\theta}\right.\\ & \left.-\frac{\cos\theta}{\sin^2\theta}\frac{\partial F_\theta}{\partial\phi}\right)\end{aligned} \tag{B.4}$$

Combining Equation (B.3) and (B.4) according to Equation (B.2) and using the definitions in Equation (B.1) leads to the following expression for the squared angular momentum operator $\mathcal{P}_\Omega\mathcal{L}^2$,

$$\begin{aligned}\mathcal{P}_\Omega\mathcal{L}^2\boldsymbol{F}(\hat{\boldsymbol{r}}) = \quad & \hat{\boldsymbol{\theta}}\left(-\nabla_\Omega^2 F_\theta + \frac{F_\theta}{\sin^2\theta} + \frac{2\cos\theta}{\sin^2\theta}\frac{\partial F_\phi}{\partial\phi}\right)\\ & \hat{\boldsymbol{\phi}}\left(-\nabla_\Omega^2 F_\phi + \frac{F_\phi}{\sin^2\theta} + \frac{2\cos\theta}{\sin^2\theta}\frac{\partial F_\theta}{\partial\phi}\right).\end{aligned} \tag{B.5}$$

Finally we recognise the ∇_Ω^2 operator from Equation (B.1),

$$\mathcal{L}^2\boldsymbol{F}(\hat{\boldsymbol{r}}) = -\nabla_\Omega^2\boldsymbol{F}(\hat{\boldsymbol{r}}).$$

Appendix C Product rules for angular momentum

The ∇^2 operator acing upon two vector fields is calculated as

$$\nabla^2(\Phi\Psi) = \nabla\cdot\nabla(\Phi\Psi) = \nabla\cdot(\Psi\nabla\Phi + \Phi\nabla\Psi) = 2\nabla\Psi\cdot\nabla\Phi + \Phi\nabla^2\Psi + \Psi\nabla^2\Phi.$$

The same principle can be applied to a tangential vector field $\boldsymbol{F}$, when it is regarded in its Cartesian components,

$$\nabla^2(\boldsymbol{F}\Psi) = 2\nabla\Psi\cdot\nabla\boldsymbol{F} + \boldsymbol{F}\nabla^2\Psi + \Psi\nabla^2\boldsymbol{F}. \tag{C.1}$$

The projection operator is expanded by its definition [2] as,

$$\nabla_\Omega^2(\boldsymbol{F}\Psi) = \boldsymbol{r}\times(\boldsymbol{r}\times\nabla^2(\boldsymbol{F}\Psi)). \tag{C.2}$$

Combining Equations (B), (C.2) and (C.1) the squared angular momentum can be written as

$$\begin{aligned}\mathcal{L}^2(\boldsymbol{F}\Psi) &= \boldsymbol{r}\times(\boldsymbol{r}\times(2\nabla\Psi\cdot\nabla\boldsymbol{F}+\boldsymbol{F}\nabla^2\Psi+\Psi\nabla^2\boldsymbol{F})\\ &= \boldsymbol{F}\mathcal{L}^2\Psi+\Psi\mathcal{L}^2\boldsymbol{F}+\boldsymbol{r}\times(\boldsymbol{r}\times(2\nabla\Psi\cdot\nabla\boldsymbol{F})).\end{aligned} \tag{C.3}$$

Hence only the last term needs further investigation,

$$r^2\nabla\Psi\cdot\nabla\boldsymbol{F} = \frac{\partial\Psi}{\partial\theta}\frac{\partial}{\partial\theta}(\hat{\boldsymbol{\theta}}F_\theta+\hat{\boldsymbol{\phi}}F_\phi)+\frac{1}{\sin^2\theta}\frac{\partial\Psi}{\partial\phi}\frac{\partial}{\partial\phi}(\hat{\boldsymbol{\theta}}F_\theta+\hat{\boldsymbol{\phi}}F_\phi) \tag{C.4}$$

By using the coordinate transformation relations [7] to cartesian coordinates one can easily prove the following relations,

$$\begin{cases}\dfrac{\partial\hat{\boldsymbol{\theta}}}{\partial\theta}=-\hat{\boldsymbol{r}},\\ \dfrac{\partial\hat{\boldsymbol{\phi}}}{\partial\theta}=0,\end{cases}\qquad\begin{cases}\dfrac{\partial\hat{\boldsymbol{\theta}}}{\partial\phi}=-\hat{\boldsymbol{\phi}}\cos\theta,\\ \dfrac{\partial\hat{\boldsymbol{\phi}}}{\partial\phi}=-\hat{\boldsymbol{\rho}}=-\hat{\boldsymbol{r}}\sin\theta-\hat{\boldsymbol{\theta}}\cos\theta.\end{cases}$$

Which are used to rewrite equation C.4,

$$\begin{aligned}r^2\nabla\Psi\cdot\nabla\mathbf{F} =& -\frac{\partial\Psi}{\partial\theta}\hat{\boldsymbol{r}}F_\theta+\frac{1}{\sin^2\theta}\frac{\partial\Psi}{\partial\phi}(\hat{\boldsymbol{\phi}}\cos\theta F_\theta-(\hat{\boldsymbol{r}}\sin\theta+\hat{\boldsymbol{\theta}}\cos\theta)F_\phi)\\ &+\frac{\partial\Psi}{\partial\theta}\left(\hat{\boldsymbol{\theta}}\frac{\partial F_\theta}{\partial\theta}+\hat{\boldsymbol{\phi}}\frac{\partial F_\phi}{\partial\theta}\right)+\frac{1}{\sin^2\theta}\frac{\partial\Psi}{\partial\phi}\left(\hat{\boldsymbol{\theta}}\frac{\partial F_\theta}{\partial\phi}+\hat{\boldsymbol{\phi}}\frac{\partial F_\phi}{\partial\phi}\right).\end{aligned} \tag{C.5}$$

This equation can then be put back into Equation C.4to make the following simplification,

$$\begin{aligned}\boldsymbol{r}\times(\boldsymbol{r}\times(2\nabla\Psi\cdot\nabla\boldsymbol{F})) =& -2\frac{\cos\theta}{\sin^2\theta}\frac{\partial\Psi}{\partial\phi}\left(\hat{\boldsymbol{\phi}}F_\theta-\hat{\boldsymbol{\theta}}F_\phi\right)-2\frac{\partial\Psi}{\partial\theta}\left(\hat{\boldsymbol{\theta}}\frac{\partial F_\theta}{\partial\theta}+\hat{\boldsymbol{\phi}}\frac{\partial F_\phi}{\partial\theta}\right)\\ &-\frac{2}{\sin^2\theta}\frac{\partial\Psi}{\partial\phi}\left(\hat{\boldsymbol{\theta}}\frac{\partial F_\theta}{\partial\phi}+\hat{\boldsymbol{\phi}}\frac{\partial F_\phi}{\partial\phi}\right),\\ =& -2\frac{\cos\theta}{\sin^2\theta}\frac{\partial\Psi}{\partial\phi}\hat{\boldsymbol{r}}\times\boldsymbol{F}-2\left(\hat{\boldsymbol{\theta}}\nabla_\Omega F_\theta+\hat{\boldsymbol{\phi}}\nabla_\Omega F_\phi\right)\cdot\nabla_\Omega\Psi.\end{aligned} \tag{C.6}$$

Thus using C.6 and C.3 the product can finally be written as:

$$\mathcal{L}^2(\boldsymbol{F}\Psi)=\boldsymbol{F}\mathcal{L}^2\Psi+\Psi\mathcal{L}^2\boldsymbol{F}-2\frac{\cos\theta}{\sin^2\theta}\frac{\partial\Psi}{\partial\phi}(\hat{\boldsymbol{r}}\times\boldsymbol{F})-2(\hat{\boldsymbol{\theta}}\nabla_\Omega F_\theta+\hat{\boldsymbol{\phi}}\nabla_\Omega F_\phi)\cdot\nabla_\Omega\Psi \tag{C.7}$$

Appendix D Translation of the far-field

Translation of the origin of the far-field can be expressed mathematically as

$$\boldsymbol{F}(\hat{\boldsymbol{r}})\rightarrow\boldsymbol{F}(\hat{\boldsymbol{r}})e^{-\mathrm{j}\boldsymbol{k}\cdot\boldsymbol{d}}.$$

Hence in the calculation of the squared angular momentum the product rules from appendix C become applicable,

$$L^2(\boldsymbol{F}(\hat{\boldsymbol{r}}),\boldsymbol{d}) = \iint_\Omega \boldsymbol{F}^*(\hat{\boldsymbol{r}})e^{\mathrm{j}\boldsymbol{k}\cdot\boldsymbol{d}} \cdot \mathcal{P}_\Omega \mathcal{L}^2 \boldsymbol{F}(\hat{\boldsymbol{r}})e^{-\mathrm{j}\boldsymbol{k}\cdot\boldsymbol{d}}\mathrm{d}\Omega. \tag{D.1}$$

The product rule for squared angular momentum acting on a vectorfield and a scalar field is given in (C.7). In this case $\Psi = e^{-\mathrm{j}\boldsymbol{k}\cdot\boldsymbol{d}}$, the derivatives of Ψ in (C.7) then become,

$$\begin{cases} \dfrac{\partial\Psi}{\partial\theta} = -\mathrm{j}k\hat{\boldsymbol{\theta}}\cdot\boldsymbol{d}e^{-\mathrm{j}\boldsymbol{k}\cdot\boldsymbol{d}}, \\ \dfrac{\partial\Psi}{\partial\phi} = -\mathrm{j}k\hat{\boldsymbol{\phi}}\cdot\boldsymbol{d}\sin\theta e^{-\mathrm{j}\boldsymbol{k}\cdot\boldsymbol{d}}, \\ \nabla_\Omega\Psi = -\mathrm{j}k\left[\hat{\boldsymbol{\theta}}\hat{\boldsymbol{\theta}} + \hat{\boldsymbol{\phi}}\hat{\boldsymbol{\phi}}\right]\cdot\boldsymbol{d}e^{-\mathrm{j}\boldsymbol{k}\cdot\boldsymbol{d}}, \\ \mathcal{L}^2[\Psi] = -\mathrm{j}2k\hat{\boldsymbol{r}}\cdot\boldsymbol{d}e^{-\mathrm{j}\boldsymbol{k}\cdot\boldsymbol{d}} + k^2\left[(\hat{\boldsymbol{\theta}}\cdot\boldsymbol{d})^2 + (\hat{\boldsymbol{\phi}}\cdot\boldsymbol{d})^2\right]e^{-\mathrm{j}\boldsymbol{k}\cdot\boldsymbol{d}}. \end{cases} \tag{D.2}$$

Using these derivatives (C.7) can be rewritten as,

$$\begin{aligned} \mathcal{L}^2(\boldsymbol{F}e^{-\mathrm{j}\boldsymbol{k}\cdot\boldsymbol{d}}) = &\Big\{\boldsymbol{F}\left(-\mathrm{j}2k\hat{\boldsymbol{r}}\cdot\boldsymbol{d} + k^2\left[(\hat{\boldsymbol{\theta}}\cdot\boldsymbol{d})^2 + (\hat{\boldsymbol{\phi}}\cdot\boldsymbol{d})^2\right]\right) \\ &+ \mathcal{L}^2\boldsymbol{F} + \mathrm{j}2k\cot\theta\hat{\boldsymbol{\phi}}\cdot\boldsymbol{d}(\hat{\boldsymbol{r}}\times\boldsymbol{F}) \\ &+\mathrm{j}2k(\hat{\boldsymbol{\theta}}\nabla_\Omega F_\theta + \hat{\boldsymbol{\phi}}\nabla_\Omega F_\phi)\cdot\left[\hat{\boldsymbol{\theta}}\hat{\boldsymbol{\theta}} + \hat{\boldsymbol{\phi}}\hat{\boldsymbol{\phi}}\right]\cdot\boldsymbol{d}\Big\}e^{\mathrm{j}\boldsymbol{k}\cdot\boldsymbol{d}}. \end{aligned}$$

This expression is then put into (4.4.3) to get the translated squared angular momentum,

$$\begin{aligned} L^2(\boldsymbol{F}(\hat{\boldsymbol{r}}),\boldsymbol{d}) = \iint_\Omega \Big\{&(\boldsymbol{F}^*\cdot\mathcal{L}^2\boldsymbol{F}) + (\boldsymbol{F}^*\cdot\boldsymbol{F})\left(k^2\left[(\hat{\boldsymbol{\theta}}\cdot\boldsymbol{d})^2 + (\hat{\boldsymbol{\phi}}\cdot\boldsymbol{d})^2\right]\right) \\ &- \mathrm{j}2k\Big((\boldsymbol{F}^*\cdot\boldsymbol{F})(\hat{\boldsymbol{r}}\cdot\boldsymbol{d}) - \cot\theta\hat{\boldsymbol{r}}\cdot(\boldsymbol{F}\times\boldsymbol{F}^*)(\hat{\boldsymbol{\phi}}\cdot\boldsymbol{d}) \\ &-(F_\theta^*\nabla_\Omega F_\theta + F_\phi^*\nabla_\Omega F_\phi)\cdot\left[\hat{\boldsymbol{\theta}}\hat{\boldsymbol{\theta}} + \hat{\boldsymbol{\phi}}\hat{\boldsymbol{\phi}}\right]\cdot\boldsymbol{d}\Big)\Big\}\,\mathrm{d}\Omega. \end{aligned}$$

Finally the expression can be rewritten to a more compact form,

$$L^2[\boldsymbol{F}(\hat{\boldsymbol{r}}),\boldsymbol{d}] = a_0 + 2k\boldsymbol{a}_1\cdot\boldsymbol{d} + k^2\boldsymbol{d}\cdot\boldsymbol{A}_2\cdot\boldsymbol{d}, \tag{D.3}$$

where

$$\begin{cases} a_0 = L^2(\boldsymbol{F}(\hat{\boldsymbol{r}}),0) = \iint_\Omega \boldsymbol{F}^*\cdot\mathcal{L}^2\boldsymbol{F}\mathrm{d}\Omega, \\ \boldsymbol{a}_1 = -\,\mathrm{j}\iint_\Omega(\boldsymbol{F}^*\cdot\boldsymbol{F})\hat{\boldsymbol{r}}\mathrm{d}\Omega + \mathrm{j}\iint_\Omega[F_\theta^*\nabla_\Omega F_\theta + F_\phi^*\nabla_\Omega F_\phi]\mathrm{d}\Omega \\ \qquad\quad + \mathrm{j}\iint_\Omega\cot\theta\hat{\boldsymbol{r}}\cdot(\boldsymbol{F}\times\boldsymbol{F}^*)\hat{\boldsymbol{\phi}}\mathrm{d}\Omega, \\ \boldsymbol{A}_2 = \iint_\Omega(\boldsymbol{F}^*\cdot\boldsymbol{F})[\hat{\boldsymbol{\theta}}\hat{\boldsymbol{\theta}} + \hat{\boldsymbol{\phi}}\hat{\boldsymbol{\phi}}]\mathrm{d}\Omega. \end{cases} \tag{D.4}$$

$\boldsymbol{a}_1$ can be further rewritten to show that it is in fact a real valued quantity. If Gauss theorem on the unit sphere [23, (A3.45)],

$$\iint_\Omega u(\hat{\boldsymbol{r}})\hat{\boldsymbol{r}}\mathrm{d}\Omega = \frac{1}{2}\iint_\Omega \nabla_\Omega u(\hat{\boldsymbol{r}})\mathrm{d}\Omega, \tag{D.5}$$

is applied to the first integral in $\boldsymbol{a}_1$ we get:

$$\begin{aligned}-\mathrm{j}\iint_\Omega (\boldsymbol{F}^*\cdot\boldsymbol{F})\hat{\boldsymbol{r}}\mathrm{d}\Omega &= -\frac{\mathrm{j}}{2}\iint_\Omega \nabla_\Omega(\boldsymbol{F}^*\cdot\boldsymbol{F})\mathrm{d}\Omega \\ &= -\frac{\mathrm{j}}{2}\iint_\Omega [F_\theta\nabla_\Omega F_\theta^* + F_\phi\nabla_\Omega F_\phi^* + F_\theta^*\nabla_\Omega F_\theta + F_\phi^*\nabla_\Omega F_\phi]\mathrm{d}\Omega.\end{aligned}$$

Which when combined with the second integral in $\boldsymbol{a}_1$ becomes,

$$\begin{aligned}&-\frac{\mathrm{j}}{2}\iint_\Omega [F_\theta\nabla_\Omega F_\theta^* + F_\phi\nabla_\Omega F_\phi^* - (F_\theta^*\nabla_\Omega F_\theta + F_\phi^*\nabla_\Omega F_\phi)]\mathrm{d}\Omega \\ &= -\frac{\mathrm{j}}{2}\iint_\Omega [F_\theta\nabla_\Omega F_\theta^* + F_\phi\nabla_\Omega F_\phi^* - (F_\theta\nabla_\Omega F_\theta^* + F_\phi\nabla_\Omega F_\phi^*)^*]\mathrm{d}\Omega \\ &= \iint_\Omega \mathrm{Im}[F_\theta\nabla_\Omega F_\theta^* + F_\phi\nabla_\Omega F_\phi^*]\mathrm{d}\Omega.\end{aligned} \tag{D.6}$$

The last integral in $\boldsymbol{a}_1$ can be written as,

$$\mathrm{j}\iint_\Omega \cot\theta\hat{\boldsymbol{r}}\cdot(\boldsymbol{F}(\hat{\boldsymbol{r}})\times\boldsymbol{F}^*(\hat{\boldsymbol{r}}))\hat{\boldsymbol{\phi}}\mathrm{d}\Omega = -2\iint_\Omega \cot\theta\ \mathrm{Im}(F_\theta F_\phi^*)\hat{\boldsymbol{\phi}}\,\mathrm{d}\Omega, \tag{D.7}$$

by explicitly calculating the cross product and projection with regards to the fields angular components. Thus when (D.6) and (D.7) are used to simplify $\boldsymbol{a}_1$ it is more apparent that $\boldsymbol{a}_1$ is real-valued,

$$\boldsymbol{a}_1 = \iint_\Omega \mathrm{Im}[F_\theta\nabla_\Omega F_\theta^* + F_\phi\nabla_\Omega F_\phi^*]\mathrm{d}\Omega - 2\iint_\Omega \mathrm{Im}F_\theta F_\phi^*\mathrm{d}\Omega.$$

Now only the $\boldsymbol{A}_2$ term in (D.4) remains to be analyzed to prove that all the quantities are positive and real valued. This can be seen by multiplying it by an arbitrary real vector $\boldsymbol{d} = d\hat{\boldsymbol{d}}$,

$$\boldsymbol{d}\cdot\boldsymbol{A}_2\cdot\boldsymbol{d} = d^2\iint_\Omega \boldsymbol{F}^*\cdot\boldsymbol{F}[(\hat{\boldsymbol{d}}\cdot\hat{\boldsymbol{\theta}})^2 + (\hat{\boldsymbol{d}}\cdot\hat{\boldsymbol{\phi}})^2]\mathrm{d}\Omega > 0. \tag{D.8}$$

Thus all quantities in (D.4) are positive real valued or positive definite and can be written as,

$$\begin{cases} a_0 = L^2(\boldsymbol{F}(\hat{\boldsymbol{r}}),0) = \iint_\Omega \boldsymbol{F}^*\cdot\mathcal{L}^2\boldsymbol{F}\,\mathrm{d}\Omega, \\ \boldsymbol{a}_1 = \iint_\Omega \mathrm{Im}[F_\theta\nabla_\Omega F_\theta^* + F_\phi\nabla_\Omega F_\phi^*]\,\mathrm{d}\Omega - 2\iint_\Omega \mathrm{Im}F_\theta F_\phi^*\,\mathrm{d}\Omega, \\ \mathbf{A}_2 = \iint_\Omega (\boldsymbol{F}^*\cdot\boldsymbol{F})[\hat{\boldsymbol{\theta}}\hat{\boldsymbol{\theta}} + \hat{\boldsymbol{\phi}}\hat{\boldsymbol{\phi}}]\,\mathrm{d}\Omega. \end{cases}$$

Appendix E Euler rotations

Euler angles are three angles that can create all rotations of an object in three dimensional space. The rotation operator based on these angles is given by

$$\mathcal{R}(\alpha,\beta,\gamma) = \begin{bmatrix} \cos\gamma\cos\alpha - \cos\beta\sin\alpha\sin\gamma & \cos\gamma\sin\alpha + \cos\beta\cos\alpha\sin\gamma & \sin\gamma\sin\beta \\ -\sin\gamma\cos\alpha - \cos\beta\sin\alpha\cos\gamma & -\sin\gamma\sin\alpha + \cos\beta\cos\alpha\cos\gamma & \cos\gamma\sin\beta \\ \sin\beta\sin\alpha & -\sin\beta\cos\alpha & \cos\beta \end{bmatrix}$$

Appendix F Simulations

The results in this thesis have been simulated using the software CST and analysing the results in Matlab. In Matlab, Ericsson Antenna Model Library toolbox has been used. CST is a powerful program used to simulate various structures including antennas. In this essay it's main use was to simulate the far-field of an antenna for a given frequency. The far-field is then exported to Matlab where the phase center calculations can be done with the eamlib toolbox.

F.1 Automating CST simulations through Matlab

Far-field data is normally not something that is simulated and exported for many different frequencies at once in CST; usually the field is only simulated for the antenna at resonance. Because of this and the fact that the far-field takes some time to simulate there is no easy way to export large amounts of far-field data from CST. The simulations done in this thesis required the full far-field for each measured frequency to determine the radiation center at that frequency. The method used to extract this data was based around running a separate CST session for each frequency. This was achieved by constructing a for loop in Matlab which created a text file specifying the parameters to be run in CST. Matlab then executed the dos-command to run CST and extracted the results. To do this some steps need to be taken to prepare the CST file which will be simulated.

1. Setup a far-field monitor which calculates the far-field at a CST variable 'freq'.
2. Run the simulation once and make sure that the far-field is displayed in the desired way by going to *plot properties*, e.g. E-field, linear scaling and origin in origo.
3. Open the Template based postprocessing window and create two tasks, "Export Farfields as Source" and "Result Storage.sdb". There are two drop down menus, the first selects your category and the second your task. To create a "Export Farfield as Source" task select the category "Farfield and Antenna Properties". When this is done an option window will appear, select the export format "ASCII .txt" and make sure the excit. string referes

to the correct far-field monitor. "Result Storage.sdb" is found in the "Misc" category and should be created without changing any default options.

F.2 Simulating single off center elements

CST is not designed to simulate elements that are moved around in reference to a fixed point. To get accurate results in CST the bounding box volume around the simulated point has to be large. The best way to ensure this is to have the bounding box be symmetric around the chosen point. When an element is moved off center the bounding box follows the element. Because of this an extra trick is needed to get accurate results. The bounding box is calculated to encapsulate objects in CST, in order to extend it more objects must be added. Since we do not want to change the simulations in any other way than to extend the dimensions of the bounding box these objects are chosen to be composed of vacuum. When CST performs a simulation it fills the area around the structure with vacuum, thus adding objects made of vacuum will not change the simulations.

The simulations in the thesis calculate the far-field in origo. When the antenna element is moved off center an inverted version of the same element made of vacuum is defined to extend the bounding box symmetrically around origo. Both these elements are then translated in opposite directions if further displacement is needed.

References

[1] IEEE145-1993. IEEE standard definition of terms for antennas, March 1993.

[2] G. Arfken. *Mathematical Methods for Physicists*. Academic Press, Orlando, third edition, 1985.

[3] C. A. Balanis. *Modern Antenna Handbook*. John Wiley & Sons, Inc., 2008.

[4] J. Friden and G. Kristensson. Calculation of antenna radiation center using angular momentum. In *Antennas and Propagation (EuCAP), 2013 7th European Conference on*, pages 1531–1535, April 2013.

[5] J. Fridén and G. Kristensson. Calculation of antenna radiation center using angular momentum. Technical Report LUTEDX/(TEAT-7219)/1–23/(2012), Lund University, Department of Electrical and Information Technology, P.O. Box 118, S-221 00 Lund, Sweden, 2012. http://www.eit.lth.se.

[6] H. Goldstein. *Classical Mechanics*. Addison-Wesley, Reading, MA, USA, second edition, 1980.

[7] D. J. Griffiths. *Introduction to Electrodynamics*. Prentice-Hall, Inc., Englewood Cliffs, New Jersey, third edition, 1999.

[8] J. Hald, J. E. Hansen, F. Jensen, and F. Holm Larsen. *Spherical Near-Field Antenna Measurements*, volume 26 of *IEE electromagnetic waves series*. Peter Peregrinus Ltd., 1998. edited by J.E. Hansen.

[9] J. E. Hansen, editor. *Spherical Near-Field Antenna Measurements*. Number 26 in IEE electromagnetic waves series. Peter Peregrinus Ltd., Stevenage, UK, 1988. ISBN: 0-86341-110-X.

[10] Y. Y. Hu. A method of determining phase centers and its application to electromagnetic horns. *Journal of the Franklin Institute*, **271**, 31 – 39, 1961.

[11] J. D. Jackson. *Classical Electrodynamics*. John Wiley & Sons, New York, second edition, 1975.

[12] R. C. Johnson. *Antenna Engineering Handbook*. McGraw-Hill, New York, third edition, 1993.

[13] G. Kristensson. *Spridningsteori med antenntillämpningar*. Studentlitteratur, Lund, 1999. (In Swedish).

[14] Y. T. Lo and S. W. Lee. *Antenna Handbook Theory, Applications and Design.* Van Nostrand Reinhold, New York, first edition, 1988.

[15] T. A. Milligan. *Modern Antenna Design, Second Edition.* John Wiley & Sons, 2005.

[16] P. M. Morse and H. Feshbach. *Methods of Theoretical Physics*, volume 2. McGraw-Hill, New York, 1953.

[17] E. I. Muehldorf. The phase center of horn antennas. *Antennas and Propagation, IEEE Transactions on*, **18**(6), 753–760, 1970.

[18] A. Neto. UWB, non dispersive radiation from the planarly fed leaky lens antenna-part I: Theory and design. *IEEE Trans. Antennas Propagat.*, **58**(7), 2238–2247, 2010.

[19] A. Neto, S. Monni, and F. Nennie. UWB, non dispersive radiation from the planarly fed leaky lens antenna-part II: Demonstrators and measurements. *IEEE Trans. Antennas Propagat.*, **58**(7), 2248–2258, 2010.

[20] P. Padilla, J. M. Fernández, J. L. Padilla, G. Expósito-Domínguez, M. Sierra-Castaner, and B. Galocha. Comparison of different methods of the experimetnal antenna phase center determination using a planar acquisition system. *Progess In Electromagnetics Research*, **135**, 331–346, 2013.

[21] J. J. Sakurai. *Modern Quantum Mechanics.* Addison Wesley, 1985.

[22] H. G. Schantz. Dispersion and uwb antennas. *2004 International Workshop on Ultra Wideband Systems, Joint with Conference on Ultrawideband Systems and Technologies. Kyoto, Japan. May 18-21*, pages 161–165, 2004.

[23] J. G. Van Bladel. *Electromagnetic Fields.* IEEE Press, Piscataway, NJ, second edition, 2007.

[24] P. D. P. W. V. T: Rusch. *Analysis of reflector antennas.* Academic press, inc. (London) LTD., 1970.

LUND
UNIVERSITY

http://www.eit.lth.se